



NTNU – Trondheim
Norwegian University of
Science and Technology

On Mimetic Finite Difference Methods for Grids with Curved Faces

Ruben Kristoffer Thomasse Bø

Master of Science in Physics and Mathematics

Submission date: June 2012

Supervisor: Helge Holden, MATH

Co-supervisor: Knut-Andreas Lie, SINTEF ICT, Department of Applied Mathematics
Stein Krogstad, SINTEF ICT, Department of Applied Mathematics

Norwegian University of Science and Technology
Department of Mathematical Sciences

Abstract

In this thesis the mimetic finite difference method for grids with curved faces is presented, implemented and tested with an emphasis on applications in reservoir simulation.

The thesis gives a brief introduction to reservoir modeling and introduce the mimetic method for flat and for curved faces. Then the continuity condition for the curved mimetic method is discussed. It is shown that the suggested continuity condition is not valid for cases with a difference in permeability between two cells separated by a curved face. An alternative continuity condition is discussed and implemented.

Numerical examples confirm that the original continuity condition is incorrect for general examples with heterogeneous permeability. Numerical examples for the alternative continuity condition shows that it is correct for simple cases, and that it gives no gain in accuracy compared to the mimetic method. In conclusion the curved mimetic method is primarily of academic interest.

Sammendrag

I denne oppgaven er mimetisk metode for grid med krumme flater presentert, implementert og testet med vekt på eksempler innen reservoarsimulering.

Oppgaven gir en kort introduksjon til reservoarsimulering og introduserer mimetisk metode for flate og krumme flater. Deretter diskuteres kontinuitetsbetingelsen for krumme flater. Det vises at denne kontinuitetsbetingelsen ikke er gyldig for grid med en diskontinuitet i permeabilitet mellom to celler som deler en krum flate. En alternativ kontinuitetsbetingelse blir presentert og implementert.

Numeriske eksempler bekrefter at den originale kontinuitetsbetingelsen ikke er gyldig for generelle tilfeller med heterogen permeabilitet. Numeriske eksempler med den alternative kontinuitetsbetingelsen bekrefter at denne er korrekt for enkle eksempler med diskontinuerlig permeabilitet, men at metoden med denne kontinuitetsbetingelsen ikke gir noen forbedring i nøyaktighet i forhold til mimetisk metode. Det konkluderes med at mimetisk metode for krumme flater primært er av akademisk interesse.

Preface

This thesis is my submission for a master's degree in the field of numerics, TMA4910, and concludes a five year study in Industrial Mathematics at the Department of Mathematical Science at the Norwegian University of Science and Technology (NTNU). It is a continuation of my specialization project, TMA4500, and is written in cooperation with SINTEF ICT, Department of Applied Mathematics.

I would like to thank my supervisor Knut-Andreas Lie at SINTEF ICT, Applied Mathematics for teaching me how to write a thesis, for answering my many emails, for detailed feedback and discussions which has been of great help. I would also like to thank my supervisor Stein Krogstad at SINTEF ICT, Applied Mathematics for helping me understand the theory, for ideas to implementation and numerical examples and invaluable input when I was stuck debugging the implementation. I would also like to thank both of you for welcoming me to the SINTEF office in Oslo, my visits there has been of great help. I would also like to thank the rest of the group at SINTEF, especially Bård Skaflestad for his expertise and help with MRST.

I would like to thank my supervisor Helge Holden at the Department of Mathematical Science, NTNU, for introducing me to SINTEF and for reading and commenting on my thesis.

Lastly I would like to thank my friends and family, especially my friends at the Department for Mathematical Science for mutual help and for making the five years at NTNU fun and enjoyable.

Contents

1	Introduction	1
2	Reservoir modeling	3
2.1	Reservoir rock	3
2.2	Equations	4
2.3	Reservoir characterization	5
2.4	Grid	6
2.5	Discretisation	7
3	Theory	13
3.1	An introduction to mimetic methods	13
3.2	An incorrect continuity condition	21
3.3	An alternative continuity condition	22
4	Implementation	25
4.1	MRST	25
4.2	The curved mimetic method	25
4.3	Boundary conditions for the mimetic method	26
4.4	Boundary conditions for curved faces	27
4.5	Grid refinement strategies	29
5	Numerical experiments and results	31
5.1	The homogeneous case	31
5.1.1	The simplest test	32
5.1.2	SBED model	37
5.2	Tests of the naive continuity condition	40
5.2.1	A simple test case	40
5.2.2	A test with curved faces	41
5.2.3	SBED model	44
5.3	Tests of the new curved mimetic method	46
5.3.1	A simple test case	46

5.3.2	A test with curved faces	47
5.4	Curved boundary condition	52
5.4.1	A simple test	52
5.4.2	A test with curved faces	53
5.5	An example with wells	56
5.5.1	The model	56
5.5.2	A first test with flat faces	56
5.5.3	A test with curved faces	58
5.5.4	A test on a perturbed grid	60
6	Conclusion and further work	63
	Bibliography	65
A	MRST module	67
A.1	The implementation in MATLAB	67
A.2	Tutorial for the CMFD module	67

Chapter 1

Introduction

Modeling of fluid flow through porous media has several applications. In this thesis the focus will be on applications for the oil and gas industry. Oil and gas is found in subsurface porous rock. Numerical models for how the oil and gas flow through this rock, are important tools for the industry. This is called reservoir simulation.

An important part of reservoir simulation is to solve an equation for the pressure. This is typically an elliptic equation. For multi-phase models, one also has a saturation equation. This is typically a hyperbolic equation. However in this thesis we will only discuss single-phase flow, and hence consider the elliptic pressure equation. The standard method for solving these equations is the two-point flux approximation (TPFA) method. This is a finite volume method, and as the name suggests, it uses two points to approximate the flux over each face, which is proportional to the pressure gradient. TPFA is only consistent for certain grid types, in particular it assumes the grid to be K-orthogonal. We will come back to what that means later.

A lot of work has been done to construct methods that are consistent on more general grids, e.g., multipoint flux approximation (MPFA) methods and mimetic methods. A common assumption for these methods is that the grid faces are flat. Real grid models used in reservoir simulation often contain cells having curved faces. Mimetic methods that are convergent for such cases have recently been developed [4]. The importance for practical simulation has not yet been thoroughly investigated.

The original aim of this thesis was to implement and investigate the accuracy and cost of the mimetic method for curved faces. However, the method suggested in [4] uses a naive continuity condition, and is only valid for some special cases. This thesis will investigate how this affects the accuracy for more realistic examples. An alternative continuity condition is also imple-

mented, and its performance is investigated.

Chapter 2

Reservoir modeling

A reservoir model consists of a description of the geometry and petrophysical properties of the rock, as well as a numerical approximation to the differential equations used to describe fluid flow. In this thesis we consider a highly simplified model: Incompressible single-phase fluid, ignoring gravity.

2.1 Reservoir rock

Reservoir rock is formed from mineral particles transported by wind and water to lakes, river deltas, etc where they settle. Layers of sediments with different mineral and rock content is gradually buried deeper and over time transform to different rock types. Over time these large flat layers are often bent, folded or displaced by geological activity, giving a complex geometry. The layers range from a decimeter scale to tens of meters in the vertical direction and can stretch across an entire reservoir in the horizontal direction. Similar rock formations are found in daylight at Svalbard, shown in Figure 2.1.

On a micrometer scale the rock have pores and channels of void space. And it is in these pores the fluid flow happen. For a small section of the reservoir we are able to model the flow on a pore scale, but we are not able to and do not aim to model on a pore scale for the whole reservoir. Instead we start with a continuum hypotheses, i.e., there exists some representative elementary volume (REV) on which the rock properties are homogeneous so that these properties can be modeled as a continuum that the fluid flows through. This means that we are able to model the rock properties as piecewise continuous functions in space. Usually we approximate the rock properties by piecewise constant functions.

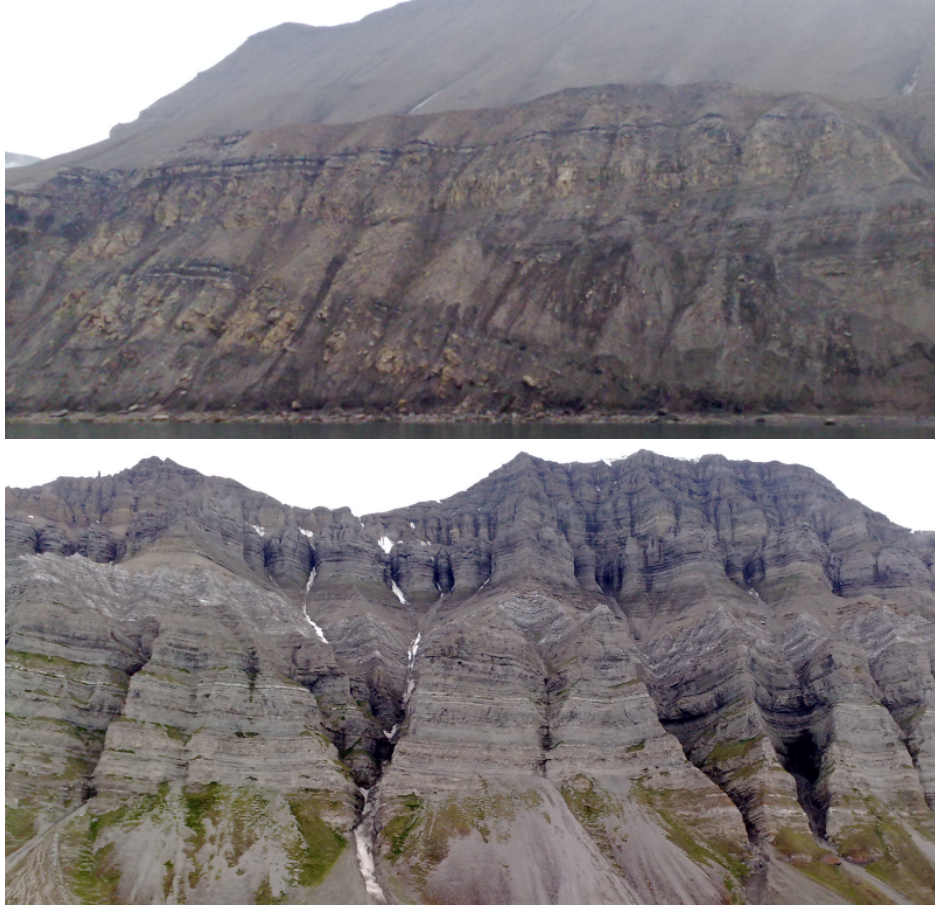


Figure 2.1: Outcrops of sedimentary rocks from Svalbard, Norway. Length scale: ~ 100 m. Photo: K.A. Lie

2.2 Equations

In this section we derive equations to describe fluid flow in porous medium. Since this thesis has a focus on the continuity condition in the mimetic method for grids with curved faces, we will not go into gravity effects, compressibility effects, or multi-phase flow. Therefore, and for the simplicity of notation, we will do simplifications on the equations in this section.

To derive equations for the fluid flow model, we start by mass conservation. We consider the Darcy velocity \vec{v} defined as the volume flux per area. Considering any subset Ω_0 of the domain Ω , the mass conservation equation is

$$\frac{\partial}{\partial t} \int_{\Omega_0} (\phi \rho) \, d\Omega + \int_{\partial\Omega_0} (\rho \vec{v}) \cdot \vec{n} \, d\sigma = \int_{\Omega_0} b \, d\Omega, \quad (2.1)$$

where ϕ is the porosity, ρ is the mass density and b is a source / sink function, typically describing wells. For incompressible fluids, ρ is independent of time, and assuming incompressible rock, ϕ is also independent of time and the first term vanish. Then, by the divergence theorem, mass conservation can be written in differential form

$$\nabla \cdot (\rho \vec{v}) = b. \quad (2.2)$$

To make notation simpler, we assume that the mass density ρ equals one.

The next step is to find an equation for the velocity in terms of pressure. Henry Darcy found a relationship from his experiments in 1856. Later it is shown that one can also derive Darcy's law from the Navier-Stokes equations. Darcy's law is analogous to Fick's law in diffusion theory and Ohm's law in electromagnetic theory, and can be written as

$$\vec{v} = -\frac{\mathbf{K}}{\mu} \nabla \Phi, \quad (2.3)$$

where \mathbf{K} is the permeability, μ is the viscosity and $\Phi = p - \rho g z$ is the pressure potential. For the single-phase case the viscosity is a constant that we henceforth will assume to be equal to one. And since we are ignoring gravity effects, Darcy's law becomes

$$\vec{v} = -\mathbf{K} \nabla p. \quad (2.4)$$

Hence we get the following set of equations

$$\nabla \cdot \vec{v} = b, \quad \vec{v} = -\mathbf{K} \nabla p. \quad (2.5)$$

2.3 Reservoir characterization

The important rock properties in a reservoir model are *porosity* and *permeability*. Porosity ϕ is the volumetric fraction of the rock that is filled with void space. Permeability \mathbf{K} is the rock's ability to transmit fluid when the rock is filled with this fluid. It is defined as the proportionality constant in Darcy's law. On a local scale the permeability is a diagonal tensor, although when doing an approximation to fit a larger scale, off-diagonal terms may appear.

Building a good description of the reservoir rock properties is an expensive and non-trivial task. Geologists use a range of techniques to determine these properties. The most important source of information is knowledge of the rock history and formation. This knowledge is obtained by studying similar rock formations in open daylight, e.g., at Svalbard, as shown on the pictures in Figure 2.1. One can also study the rock by X-ray or in an electron microscope. This can give an understanding of the size, connectedness and distribution of the pores. Measurement of the flow versus pressure drop on samples from well drilling will give an understanding of the permeability in and around the well. Seismic data is another source of information. These techniques give different information on different scales. On seismic data, one can not expect to see formations that are thinner than 10 meters. Likewise, it is obviously not possible to get a full model of the rock pores on a micrometer scale for the whole reservoir. It is also not necessary. In a reservoir model it is sufficient to determine the general flow patterns.

2.4 Grid

In order to represent the reservoir volume and the rock properties discussed above, we partition the total reservoir volume into non-overlapping polyhedral cells. Let $\Omega \subset \mathbb{R}^3$ be the total volume and Ω_h the partitioning of Ω . This partitioning is called the grid.

The grid cells are defined by its *vertices* (corner points), *edges* connecting pairs of vertices and *faces*. A face is defined by a subset of vertices, and it defines a connection between two neighboring cells. We assume the grids to be *conforming*, i.e., that each internal face defines the connection between exactly two faces. Note that grids that are non-conforming, can be made conforming by introducing new edges and/or vertices. How the cells are connected is called the *topology* of the grid.

The simplest grids are *regular Cartesian grids*, that is when all cells are unit cubes. If the grid consists of rectangular cuboids, we call it a *rectilinear grid*. A *curvilinear grid* is a grid that has the same topology as a regular Cartesian grid, but where the cells are cuboids rather than cubes. A 2D illustration is made in Figure 2.2. Note that a cuboid defined by eight points in space need not have planar faces. However it is a common assumption for numerical methods, that the grid cells do have planar faces. Depending on the numerical method used, the grid cells will satisfy certain regularity conditions. We will come back to that later.

On a grid, the permeability tensor \mathbf{K} is represented as a symmetric matrix for each cell. In other words, we are assuming \mathbf{K} to be constant on

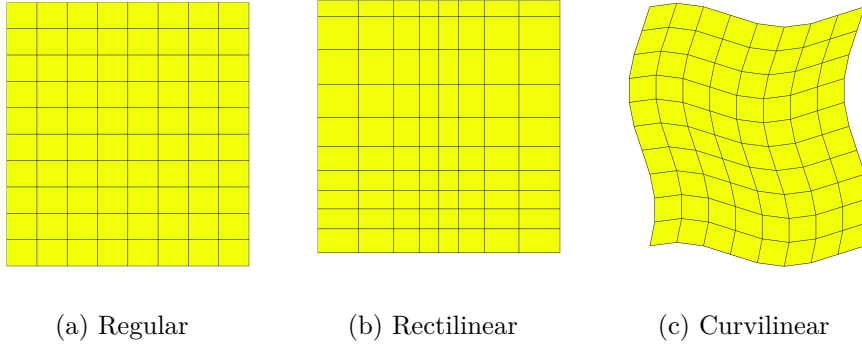


Figure 2.2: Grid types

each grid cell. As mentioned, it is common that the permeability tensor is diagonal, resulting in one diagonal permeability matrix for each cell. Two things that are important when choosing a grid, are: First one wish to match the rock properties as good as possible, i.e., to minimize the error made by approximating the rock properties to be constant on each grid cell. Second, one must consider the assumptions the numerical method makes on the grid. For instance, a regular Cartesian grid will make the construction of a numerical solver easy, but will not match the rock properties as good as grids with more complex geometries.

2.5 Discretisation

Next we need a numerical approximation method to Equation (2.5). To this end there are several choices. In this section we introduce a general framework for finite volume method. Then we introduce the two-point flux approximation method.

General finite volume methods

We want to build a general finite volume discretization for Equation (2.5). First we require the discretization to be locally conservative, i.e., conserving mass in each cell. We also want the discretization to be exact for linear pressure fields. For each cell i we introduce the pressure at the cell centroid p_i , the Darcy flux $v_{i,e}$ over each face e , and the pressure $\pi_{i,e}$ at each face centroid. For most methods, one degree of freedom per face is used for the Darcy flux, i.e., one approximates the flux over each face by the normal

component of the velocity. Note that the curved mimetic method introduces extra degrees of freedom on curved faces.

General finite-volume methods and mimetic methods can be written in the general form

$$\mathbf{v}_i = \mathbf{T}_i (\mathbf{e}_i p_i - \boldsymbol{\pi}_i), \quad \mathbf{e}_i = (1, \dots, 1)^T. \quad (2.6)$$

for each cell i , where the elements of \mathbf{v}_i are the Darcy flux over each face. Local conservation can be written $\sum_e (v_i)_e = b_i$ for all cells i . Requiring continuity for all internal faces e shared by cells i and j gives $(v_i)_e = -(v_j)_e$. Equation (2.6) together with local conservation and continuity can be written on the following matrix form

$$\begin{bmatrix} \mathbf{B} & \mathbf{C} & \mathbf{D} \\ \mathbf{C}^T & \mathbf{0} & \mathbf{0} \\ \mathbf{D}^T & \mathbf{0} & \mathbf{0} \end{bmatrix} \begin{bmatrix} \mathbf{v} \\ -\mathbf{p} \\ \boldsymbol{\pi} \end{bmatrix} = \begin{bmatrix} \mathbf{0} \\ \mathbf{b} \\ \mathbf{0} \end{bmatrix}, \quad (2.7)$$

where $\mathbf{C} \in \mathbb{R}^{N_e \times N}$ is a matrix where each row corresponds to a cell, having ones at the corresponding faces; \mathbf{B} is a block diagonal matrix of the \mathbf{T}_i^{-1} 's; and \mathbf{D} is a matrix where each column corresponds to a face, having ones at the corresponding faces, i.e., two non-zero entries for the internal faces and one for boundary faces. The first row, $\mathbf{B}\mathbf{v} - \mathbf{C}\mathbf{p} + \mathbf{D}\boldsymbol{\pi} = \mathbf{0}$, corresponds to Darcy's law. The second, $\mathbf{C}^T\mathbf{v} = \mathbf{b}$, corresponds to mass conservation and the last row, $\mathbf{D}^T\mathbf{v} = \mathbf{0}$ asserts that the flux over internal faces are consistent.

Two-point flux approximation (TPFA)

In this subsection we present the two-point flux approximation (TPFA) method [1]. This is a finite volume method, but since it is cell centered one need not put it into the framework of Equation (2.7). Instead it is set up to calculate the cell pressures directly, and the face pressures and fluxes can be reconstructed from this.

To construct the TPFA method, we start by considering each cell Ω_i as a control volume, i.e., apply Equation (2.1) on each cell. Assuming we are not at a well, we get

$$\sum_{e=1}^{N_e} \int_e (\vec{v} \cdot \vec{n}) d\sigma = \sum_{e=1}^{N_e} v_e = 0, \quad (2.8)$$

where N_e is the number of faces for each cell, and v_e is an approximation to the flux across each face e . We consider the grid cells shown in Figure 2.3, and consider only the flow across face e , i.e., the flow from cell i to cell j . The other directions are analogous.

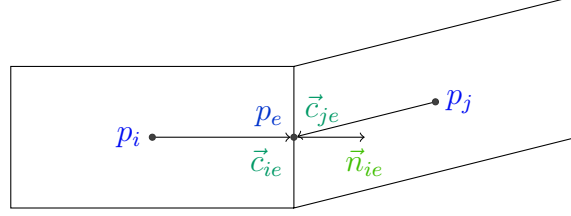


Figure 2.3: Grid cells used to describe the TPFM method. p_i and p_j are the cell pressures, p_e is the face pressure, \vec{n}_{ie} is the normal vector of face e out of cell i and \vec{c}_{ie} and \vec{c}_{je} are vectors from the cell centroid to the face centroid.

Let \mathbf{K}_e and v_e denote the permeability and Darcy velocity at face e , respectively. Then we use Darcy's law (2.4) to obtain an expression for the flux

$$v_e = \int_e -\mathbf{K}_e \nabla p \cdot \vec{n}_e \, d\sigma, \quad (2.9)$$

which can be written

$$v_e = \int_e -\mathbf{K}_e \vec{n}_e \cdot \nabla p \, d\sigma, \quad (2.10)$$

since \mathbf{K} is symmetric. The integrand is the directional derivative of the pressure in the direction of $\mathbf{K}_e \vec{n}_e$.

Since the permeability is defined to be constant within each cell, we do not know the value of the permeability at the face, \mathbf{K}_e , explicitly. We do however have the permeability in each cell, so we start by considering the flux v_e from each of the cells separately

$$v_{e,l} = \int_e -\mathbf{K}_l \vec{n}_e \cdot \nabla p \, d\sigma, \quad l = i, j, \quad (2.11)$$

where $v_{e,i}$ and $v_{e,j}$ are the flux seen from cell i and j respectively. To do an approximation, we introduce a pressure potential p_e at a fictitious point x_e on e . This can be approximated as follows

$$\begin{aligned}
v_{e,i} &\approx -|e|(p_e - p_i) \frac{\|\mathbf{K}_i \vec{n}_e\|}{\|\vec{c}_{ie}\|} \\
v_{e,j} &\approx -|e|(p_e - p_j) \frac{\|\mathbf{K}_j \vec{n}_e\|}{\|\vec{c}_{je}\|}.
\end{aligned} \tag{2.12}$$

if and only if $\mathbf{K}_l \vec{n}_e$ is parallel to \vec{c}_{le} for $l = i, j$ [?]. Eliminating p_e by subtracting $(p_e - p_i) - (p_e - p_j)$ in the equations above, we get

$$|e|(p_j - p_i) = v_{e,i} \frac{\|\vec{c}_{ie}\|}{\|\mathbf{K}_i \vec{n}_e\|} - v_{e,j} \frac{\|\vec{c}_{je}\|}{\|\mathbf{K}_j \vec{n}_e\|}. \tag{2.13}$$

Since the flux must be the same with opposite signs when seen from the two sides, we have $v_{e,i} = -v_{e,j}$, and get

$$v_{ij} = |e_{ij}| \left(\frac{\|\vec{c}_{ie}\|}{\|\mathbf{K}_i \vec{n}_e\|} + \frac{\|\vec{c}_{je}\|}{\|\mathbf{K}_j \vec{n}_e\|} \right)^{-1} (p_j - p_i). \tag{2.14}$$

To set up the full system for the pressure unknowns, we introduce the face transmissibilities defined by

$$t_{ij} = |e_{ij}| \left(\frac{\|\vec{c}_{ie}\|}{\|\mathbf{K}_i \vec{n}_e\|} + \frac{\|\vec{c}_{je}\|}{\|\mathbf{K}_j \vec{n}_e\|} \right)^{-1}, \tag{2.15}$$

This gives

$$\sum_{j=1}^{N_e} t_{ij} (p_i - p_j) = \int_{\Omega_i} b dx, \tag{2.16}$$

for all cells.

A more direct way to look at the two-point flux approximation is to look at Equation (2.10) and use the following approximation to the pressure gradient

$$\nabla p \approx \frac{(p_j - p_i)}{(\|\vec{c}_{ie}\| + \|\vec{c}_{ej}\|)} \hat{c}_{ij}. \tag{2.17}$$

where \hat{c}_{ij} is the unit vector in the direction of \vec{c}_{ij} which is the vector from the centroid of cell i to the centroid of cell j , or $\vec{c}_{ie} + \vec{c}_{ej}$.

Inserting Equation (2.17) into Equation (2.10) and comparing that to Equation (2.14) we can interpret the following harmonic average as the effective permeability at the face e

$$k_e = (\|\vec{c}_{ie}\| + \|\vec{c}_{ej}\|) \left(\frac{\|\vec{c}_{ie}\|}{\|\mathbf{K}_i \vec{n}_e\|} + \frac{\|\vec{c}_{je}\|}{\|\mathbf{K}_j \vec{n}_e\|} \right)^{-1}. \tag{2.18}$$

Note that the condition that $\mathbf{K}_l \vec{n}_e$ is parallel to \vec{c}_{le} means that the grid must be \mathbf{K} -orthogonal [2]. Another, and perhaps more common, way to define \mathbf{K} -orthogonality is to require

$$\vec{n}_k \mathbf{K} \vec{n}_l = 0 \quad (2.19)$$

for all non-parallel normal vectors \vec{n}_k and \vec{n}_l to a cell with permeability \mathbf{K} .

Chapter 3

Theory

In this chapter we introduce the mimetic method and the curved mimetic method. Then the continuity condition proposed in [5] is discussed, and an alternative continuity condition is proposed.

3.1 An introduction to mimetic methods

Mimetic finite-difference methods have been developed to be convergent for very general grids. The first version [6] assumes the grid cells to be polyhedrons with flat faces, whereas the second version [5] allows polyhedral cells with highly curved faces. However, as we will see, the second method is not valid for general examples with heterogeneous permeability.

In this section we start by introducing the mimetic method for curved faces and the standard mimetic method. Since the curved mimetic method is built based on the mimetic method, we have chosen to introduce the curved mimetic method and point out what terms are omitted to get the mimetic method.

Notation and definitions

We will need some notation and definitions for the curved mimetic method. First we introduce the average area weighted normal vector

$$\tilde{\mathbf{n}}_E^e = \int_e \vec{n}_E^e d\sigma, \quad (3.1)$$

and the unit normal

$$\mathbf{a}_E^{e,1} = \frac{\tilde{\mathbf{n}}_E^e}{|\tilde{\mathbf{n}}_E^e|} \quad (3.2)$$

where \vec{n}_E^e is the continuous outer unit normal vector to the face e . Note that $|\vec{n}_E^e| \leq |e|$ with equality only when the face is flat. We can then define a face e to be *moderately curved* if

$$\|\vec{n}_E^e - \mathbf{a}_E^{e,1}\| \leq \sigma_* \sqrt{|e|} \quad (3.3)$$

for every point on e and some chosen σ_* independent of E and e . Faces that are not moderately curved are called *strongly curved*. For each face we will use the notation

$$\sigma = \max_{\vec{x} \in e} \frac{\|\vec{n}_E^e(\vec{x}) - \mathbf{a}_E^{e,1}\|}{\sqrt{|e|}} \quad (3.4)$$

to characterize the curvature of the face.

Note that the mimetic method is equivalent to the curved mimetic method on a grid where all faces are moderately curved.

We will also need a local coordinate system for each face. Let $\mathbf{a}_E^{e,2}$ and $\mathbf{a}_E^{e,3}$ be unit vectors that are mutually orthogonal and orthogonal to $\mathbf{a}_E^{e,1}$. As for the direction of the normal vectors, we require $\mathbf{a}_{E_1}^{e,i} = -\mathbf{a}_{E_2}^{e,i}$ for each face e shared by two cells E_1 and E_2 .

An introduction to mimetic methods on polyhedral and generalized polyhedral grids

The idea of a mimetic finite-difference method is to mimic basic operators and theorems in vector calculus. For our equation this means to mimic the divergence and gradient operators, and the Greens divergence theorem. To this end, we will build a method that is exact for linear pressure fields.

Following [3] and [4] we start by defining the following inner products

$$(\vec{u}, \vec{v})_X = \int_{\Omega} \vec{u} \cdot \mathbf{K}^{-1} \vec{v} dV, \quad (3.5)$$

and

$$(p, q)_Q = \int_{\Omega} pq dV, \quad (3.6)$$

in the space X of velocities and the space Q of pressures, respectively. Using the divergence theorem we get

$$(\vec{v}, -\mathbf{K} \nabla p)_X = (p, \nabla \cdot \vec{v})_Q. \quad (3.7)$$

And we can consider the operator $\mathcal{G} := -\mathbf{K}\nabla p$ as the adjoint to the divergence operator with respect to the above inner products.

In our numerical approximation we consider a discrete pressure space Q^h as the set of all functions being constant on each grid cell. We write $\mathbf{p} \in Q^h$ and the elements of \mathbf{p} as $(\mathbf{p})_E$ or p_E . In practice we treat \mathbf{p} as elements of \mathbb{R}^{N_Q} , where N_Q is the number of polyhedrons in Ω_h . This space is used both for the mimetic and for the curved mimetic method.

Let X^h be the space of discrete flux unknowns. We will use face fluxes rather than velocities, i.e., with units volume per time through each face, since that is how it is implemented in MRST¹. We write $\mathbf{u} \in X^h$. For the curved mimetic method the elements of \mathbf{u} is defined as $u_E^{e,j}$, where $u_E^{e,1}$ is the flux over face e out of cell E and $u_E^{e,j}$, $j = 2, 3$ are extra degrees of freedom related to the orthonormal vectors $\mathbf{a}_E^{e,j}$. For the mimetic method, there is no extra degrees of freedom, and we write u_E^e for $u_E^{e,1}$. Again we will consider \mathbf{u} as elements of the subspace of \mathbb{R}^{N_X} satisfying Equation (3.8), where N_X is twice the number of internal faces plus the number of boundary faces for the mimetic case.

For the curved mimetic case, N_X is six times the number of strongly curved internal faces plus twice the number of moderately curved internal faces plus three times the number of strongly curved boundary faces plus the number of moderately curved boundary faces. We will come back to how boundary conditions are treated in Section 4.4, for the moment we assume that all boundary faces are moderately curved.

Altogether we have $N_Q + N_X$ degrees of freedom.

For the mimetic method we get the following continuity condition for all internal faces e shared by cells E_1 and E_2

$$u_{E_1}^e = -u_{E_2}^e. \quad (3.8)$$

For the curved mimetic method, it was suggested in [5] to use the following continuity condition

$$u_{E_1}^{e,j} = -u_{E_2}^{e,j}, \quad j = 1, 2, 3. \quad (3.9)$$

However, this continuity condition is only valid if E_1 and E_2 have the same permeability. We will come back to this in Section 3.2.

Now we define inner products for the discrete spaces Q^h and X^h . For the pressure, this is fairly straight forward. We take the Euclidean inner product scaled with the cell volumes $|E|$,

¹See Section 4.1

$$[\mathbf{p}, \mathbf{q}]_{Q^h} = \sum_{E \in \Omega_h} p_E q_E |E|. \quad (3.10)$$

For the discrete flux, we define the inner product cell-wise

$$[\mathbf{u}, \mathbf{v}]_{X^h} = \sum_{E \in \Omega_h} [\mathbf{u}, \mathbf{v}]_E, \quad (3.11)$$

where the inner product on each cell is given by a symmetric positive definite matrix $\mathbf{M}_E \in \mathbb{R}^{n_E \times n_E}$,

$$[\mathbf{u}, \mathbf{v}]_E = \sum_{s,r=1}^{n_E} \mathbf{M}_{E,s,r} u_E^s v_E^r. \quad (3.12)$$

For the mimetic method, $n_E = k_E$ where k_E is the number of faces for each cell. For the curved mimetic method, $n_E = l_E$ where l_E is three times the number of strongly curved faces plus the number of moderately curved faces. Some regularity is required on the matrices \mathbf{M}_E that we will come back to later. Note that in [3] and [4] they use velocities instead of fluxes, resulting in different inner products \mathbf{M} . However the conversion is trivial, one only needs to pre- and post multiply by the inverse of the area for each face, see [7].

The next step in building the mimetic method is to define discrete divergence and gradient operators. Following the divergence theorem, we define

$$(\mathcal{DIV}^h \mathbf{u})_E = \frac{1}{|E|} \sum_{s=1}^{k_E} u_E^{e_s}. \quad (3.13)$$

This is valid for both the mimetic and the curved mimetic method, where the u^{e_s} 's are the unknowns associated with the normal direction. Then we define the gradient as the adjoint of the divergence operator in our discrete inner products,

$$[\mathbf{u}, \mathcal{G}^h \mathbf{p}]_{X^h} = [\mathbf{p}, \mathcal{DIV}^h \mathbf{u}]_{Q^h} \quad \forall \mathbf{p} \in Q^h \quad \forall \mathbf{u} \in X^h. \quad (3.14)$$

Following this notation, a discrete version of Equation (2.5) should be

$$\mathcal{DIV}^h \mathbf{u} = \mathbf{b}, \quad \mathbf{u} = \mathcal{G}^h \mathbf{p}. \quad (3.15)$$

To motivate why (3.15) is an approximation of (2.5), we start by defining some interpolation operators. Given a pressure field p , let

$$(p)_E^I = \frac{1}{|E|} \int_E p \, d\Omega, \quad (3.16)$$

and for the velocity field \vec{v} we interpolate from the continuous velocity space to the discrete flux space. Let

$$((\vec{v})^I)_E^{e,j} = \int_e \vec{v} \cdot \vec{\alpha}_E^{e,j} \, d\sigma, \quad j = 1, 2, 3. \quad (3.17)$$

where

$$\vec{\alpha}_E^{e,j} = \begin{cases} \vec{n}_E^e, & j = 1 \\ \mathbf{a}_E^{e,2}, & j = 2 \\ \mathbf{a}_E^{e,3}, & j = 3. \end{cases} \quad (3.18)$$

Then we can derive [3]

$$(\mathcal{DIV}^h(\vec{v})^I)_E = \frac{1}{|E|} \sum_{s=1}^{k_E} \int_{e_s} \vec{v} \cdot \vec{n}_E^{e_s} \, dS \stackrel{Gauss}{=} \frac{1}{|E|} \int_E \nabla \cdot \vec{v} \, d\Omega = (\nabla \cdot \vec{v})_E^I. \quad (3.19)$$

This equation is valid for both the mimetic and the curved mimetic method, since the discrete divergence operator only considers the unknowns associated with the normal direction, and these unknowns are equivalent for the two methods.

The consistency assumptions in [3] and [4] can be motivated by demanding the discrete divergence and gradient operators to satisfy the divergence theorem in each cell,

$$\int_E \vec{v} \cdot \nabla p \, d\Omega + \int_E p (\nabla \cdot \vec{v}) \, d\Omega = \sum_{s=1}^{k_E} \int_{e_s} p \vec{v} \cdot \vec{n}_E^{e_s} \, d\sigma. \quad (3.20)$$

This can be rewritten to

$$(\vec{v}|_E, \mathbf{K} \nabla p|_E)_X + \int_E p (\nabla \cdot \vec{v}) \, d\Omega = \sum_{s=1}^{k_E} \int_{e_s} p \vec{v} \cdot \vec{n}_E^{e_s} \, d\sigma. \quad (3.21)$$

Let us define a discrete vector for each cell, representing the numerical velocity

$$\mathbf{u}_E^e = \frac{v_E^{e,1}}{|\vec{n}_E^e|} \mathbf{a}_E^{e,1} + \frac{v_E^{e,2}}{|e|} \mathbf{a}_E^{e,2} + \frac{v_E^{e,3}}{|e|} \mathbf{a}_E^{e,3} \quad (3.22)$$

for the curved mimetic method and simply

$$\mathbf{u}_E^e = \frac{v_E^e}{|\tilde{\mathbf{n}}_E^e|} \mathbf{a}_E^{e,1} \quad (3.23)$$

for the mimetic method. For the discrete case Equation (3.21) means we want to satisfy the following consistency condition

(Consistency condition). For any $\mathbf{v} \in X^h$ and any linear pressure field $p = \vec{a} \cdot \vec{x} + b$

$$\left[\mathbf{v}, (\mathbf{K} \nabla p)^I \right]_E + \int_E p (\mathcal{D}\mathcal{I}\mathcal{V}^h \mathbf{v})_E \, d\Omega = \sum_{s=1}^{k_E} \int_{e_s} p \mathbf{u}_E^{e_s} \cdot \vec{\mathbf{n}}_E^{e_s} \, d\sigma, \quad (3.24)$$

Looking at each space dimension $i = 1, \dots, d$ separately, the left hand side reads

$$\text{LHS} = a_i \left[\mathbf{v}, (\mathbf{K} \nabla x_i)^I \right]_E + \int_E (a_i x_i + b) (\mathcal{D}\mathcal{I}\mathcal{V}^h \mathbf{v})_E \, d\Omega. \quad (3.25)$$

Using the definition of the discrete divergence, Equation (3.13), we get

$$\text{LHS} = a_i \left[\mathbf{v}, (\mathbf{K} \nabla x_i)^I \right]_E + a_i \frac{1}{|E|} \sum_{s=1}^{k_E} v_E^{e_s} \int_E x_i \, d\Omega + b \sum_{s=1}^{k_E} v_E^{e_s}. \quad (3.26)$$

The middle term can be omitted using a symmetry argument assuming the cell center to be at origo. This assumption is ok, since we can assume frame invariance. We get

$$\text{LHS} = a_i \left[\mathbf{v}, (\mathbf{K} \nabla x_i)^I \right]_E + b \sum_{s=1}^{k_E} v_E^{e_s}. \quad (3.27)$$

The right hand side of Equation (3.24) reads

$$\text{RHS} = \sum_{s=1}^{k_E} \int_{e_s} (a_i x_i + b) \left(\frac{v_E^{e,1}}{|\tilde{\mathbf{n}}_E^e|} \mathbf{a}_E^{e,1} + \frac{v_E^{e,2}}{|e|} \mathbf{a}_E^{e,2} + \frac{v_E^{e,3}}{|e|} \mathbf{a}_E^{e,3} \right) \cdot \vec{\mathbf{n}}_E^{e_s} \, d\sigma. \quad (3.28)$$

Since the \mathbf{a}_E^e 's, the v_E^e 's and b are constants, the dot product with the continuous normal vector becomes the dot product with the average normal vector. Then by orthogonality we get

$$\text{RHS} = \sum_{s=1}^{k_E} a_i \int_{e_s} x_i \left(\frac{v_E^{e,1}}{|\tilde{\mathbf{n}}_E^e|} \mathbf{a}_E^{e,1} + \frac{v_E^{e,2}}{|e|} \mathbf{a}_E^{e,2} + \frac{v_E^{e,3}}{|e|} \mathbf{a}_E^{e,3} \right) \cdot \vec{\mathbf{n}}_E^{e_s} d\sigma + b \sum_{s=1}^{k_E} v_E^{e_s}. \quad (3.29)$$

Now we simplify the notation by including all the term in one sum;

$$\text{RHS} = \sum_{t=1}^{l_E} a_i \int_{e_t} x_i \frac{1}{\beta_E^t} v_E^t \mathbf{a}_E^t \cdot \vec{\mathbf{n}}_E^{e_t} d\sigma + b \sum_{s=1}^{k_E} v_E^{e_s}, \quad (3.30)$$

where \mathbf{a}_E^t , $t = 1, \dots, l_E$ is some numbering of the unknowns $\mathbf{a}_E^{e_s, j}$, $s = 1, \dots, k_E$ and $j = 1$ for moderately curved faces and $j = 1, 2, 3$ for strongly curved faces. And

$$\beta_E^{e_s, j} = \begin{cases} |\tilde{\mathbf{n}}_E^{e_s}|, & j = 1 \\ |e_s|, & j = 2 \\ |e_s|, & j = 3. \end{cases} \quad (3.31)$$

Equation (3.27) and (3.30) are the left and right hand side of Equation (3.24) respectively. Subtracting $b \sum_{s=1}^{k_E} v_E^{e_s}$ from both sides and dividing by a_i we get

$$\begin{aligned} \text{LHS} &= \text{RHS} \\ [\mathbf{v}, (\mathbf{K} \nabla x_i)^I]_E &= \sum_{t=1}^{l_E} v_E^t \frac{1}{\beta_E^t} \int_{e_s} x_i \mathbf{a}_E^t \cdot \vec{\mathbf{n}}_E d\sigma, \end{aligned} \quad (3.32)$$

which for flat faces simplifies to

$$[\mathbf{v}, (\mathbf{K} \nabla x_i)^I]_E = \sum_{s=1}^{k_E} v_E^{e_s} \frac{1}{|e_s|} \int_{e_s} x_i d\sigma. \quad (3.33)$$

Let \mathbf{k}_i be the i -th column of \mathbf{K} . Now let us define \mathbf{N} as the matrix with $(\mathbf{n}_E^t)^T$ as the rows; let \mathbf{C} be the matrix with $(\mathbf{c}_E^t)^T$ as rows, where $(\mathbf{c}_E^t)_i = \frac{1}{\beta_E^t} \int_{e_t} x_i \mathbf{a}_E^t \cdot \vec{\mathbf{n}}_E d\sigma$ and

$$\mathbf{n}_E^t = \beta_E^t \mathbf{a}_E^t \quad (3.34)$$

Then we can write Equation (3.32) as

$$\mathbf{v}^T \mathbf{M} \left(\int_{e_s} \mathbf{K} \nabla x_i \cdot \vec{\alpha}_E^t d\sigma \right)_{t=1}^{l_E} = \sum_{t=1}^{l_E} v_E^t \frac{1}{\beta_E^t} \int_{e_s} x_i \mathbf{a}_E^t \cdot \vec{\mathbf{n}}_E d\sigma, \quad (3.35)$$

where $(\cdot)_{t=1}^{l_E}$ denotes a column vector of length l_E . By definition of \mathbf{k}_i , \mathbf{n}_E^s and \mathbf{c}_E^t this simplifies to

$$\begin{aligned} \mathbf{v}^T \mathbf{M} (\mathbf{k}_i \cdot \mathbf{n}_E^s)_{s=1}^{l_E} &= \sum_{t=1}^{l_E} v_E^t (\mathbf{c}_E^t)_i \\ \mathbf{v}^T \mathbf{M} \mathbf{N} \mathbf{K} &= \mathbf{v}^T \mathbf{C}. \end{aligned} \quad (3.36)$$

Since this is valid for all $\mathbf{v} \in X^h$ we get

$$\mathbf{M} \mathbf{N} \mathbf{K} = \mathbf{C}. \quad (3.37)$$

For the mimetic method, this consistency condition can be derived [7] within the framework of Equation (2.6) and $\mathbf{M} = \mathbf{T}^{-1}$. For the linear pressure field $p = \vec{a} \cdot \vec{x} + b$, Darcy's law becomes $\vec{v} = -\mathbf{K}\vec{a}$. Then we get $\mathbf{v} = -\mathbf{n}\mathbf{K}\vec{a}$ for each cell. Inserting this, together with $p_E - \pi_e = \mathbf{c}_E^e \cdot \vec{a}$ into Equation (2.6) we get

$$\mathbf{M} \mathbf{N} \mathbf{K} = \mathbf{C}.$$

The following property is valid both for the mimetic [6] and the curved mimetic [5] method

$$\mathbf{C}^T \mathbf{N} = \text{diag}(|E|). \quad (3.38)$$

Following [7] we multiply Equation (3.37) by $\mathbf{K}^{-1} \mathbf{C}^T \mathbf{N}$

$$\mathbf{M} \mathbf{N} = \frac{1}{|E|} \mathbf{C} \mathbf{K}^{-1} \mathbf{C}^T \mathbf{N}. \quad (3.39)$$

Since \mathbf{N} (and \mathbf{C}) has full rank [6, 5], Equation (3.39) is equivalent to

$$\mathbf{M} = \frac{1}{|E|} \mathbf{C} \mathbf{K}^{-1} \mathbf{C}^T + \mathbf{M}_2, \quad (3.40)$$

for any \mathbf{M}_2 such that \mathbf{M} is symmetric positive definite and $\mathbf{M}_2 \mathbf{N} = \mathbf{0}$. In particular, for any symmetric positive definite matrix \mathbf{S}_M we can use

$$\mathbf{M} = \frac{1}{|E|} \mathbf{C} \mathbf{K}^{-1} \mathbf{C}^T + \mathbf{Q}_N^\perp \mathbf{S}_M \mathbf{Q}_N^{\perp T}, \quad (3.41)$$

where \mathbf{Q}_N^\perp is an orthonormal basis for the null space of \mathbf{N}^T . A similar calculation can be made for $\mathbf{T} = \mathbf{M}^{-1}$.

$$\mathbf{T} = \frac{1}{|E|} \mathbf{N} \mathbf{K} \mathbf{N}^T + \mathbf{Q}_C^\perp \mathbf{S}_T \mathbf{Q}_C^{\perp T}, \quad (3.42)$$

where \mathbf{Q}_C^\perp is an orthonormal basis for the null space of \mathbf{C}^T , and \mathbf{S}_T is any symmetric positive definite matrix.

To see how this can be set up as a linear system, we consider

$$\begin{aligned} [\mathbf{u}, \mathbf{v}]_{X^h} &= [\mathcal{G}^h \mathbf{p}, \mathbf{v}]_{X^h} \quad \forall \mathbf{v} \in X^h \\ \sum_E \mathbf{u}_E^T \mathbf{M}_E \mathbf{v}_E &= [\mathcal{D}\mathcal{I}\mathcal{V}^h \mathbf{v}, \mathbf{p}]_{Q^h} \\ \sum_E \mathbf{u}_E^T \mathbf{M}_E \mathbf{v}_E - p_E \mathbf{e}_E^T \mathbf{v}_E &= 0, \end{aligned} \quad (3.43)$$

where $\mathbf{e} = (1, \dots, 1, 0, \dots, 0)^T$ is the vector with ones as the first k_E entries and zeroes in the $2k_E$ last entries for the curved mimetic method. For the mimetic method it is simply $\mathbf{e} = (1, \dots, 1)^T$. This can be rewritten into

$$\sum_E \mathbf{M}_E \mathbf{u}_E - \mathbf{e}_E p_E + \mathbf{w}_E = 0, \quad (3.44)$$

where $\mathbf{w} \in \mathbb{R}^{N_x}$ is a new unknown satisfying $\sum_E \mathbf{w}^T \mathbf{v} = 0 \quad \forall \mathbf{v} \in X^h$. This is satisfied if $w_{E_1}^{e,j} = w_{E_2}^{e,j}$ for all components j of all faces e shared by two cells E_1 and E_2 .

This equation can be rewritten into the form of the first line in Equation (2.7), where \mathbf{B} is constructed as block diagonal with \mathbf{M}_E as its blocks. We note that the interpretation of the new unknowns \mathbf{w} will be the face pressures $\boldsymbol{\pi}$ for the mimetic method. For the curved mimetic method, an exact formula for the extra unknowns is given in [8]. The rest of Equation (2.7) is straight forward.

3.2 An incorrect continuity condition

As mentioned, the curved mimetic method suggested in [4] is not valid for general examples with heterogeneous permeability. In particular, one can not have difference in permeability in two cells separated by a strongly curved face. In this section we show why this is so. Numerical examples that verify this is done in Section 5.2.

The original mimetic method has one unknown for the flux per cell face, that is the velocity in the outer normal direction integrated over (or multiplied by) the area. As a constraint, the two unknowns associated with the same global face, i.e., when seen from the two neighboring cells, must be the same but with opposite sign. This comes from mass conservation. The curved mimetic method suggested in [4] introduces two new unknowns for

the velocity for each strongly curved face. For simplicity we now define all non-planar faces as strongly curved, i.e., setting the constant $\sigma_* = 0$ in Equation (3.3) and introduce new unknowns also for planar faces. Or think of a close to planar face that has been defined as strongly curved. If the permeability is the same for the two neighboring cells, continuity of the pressure gradient and continuity of the velocity is equivalent by Darcy's law. It is also well documented that the curved mimetic method works well for homogeneous permeability, see e.g. Section 5.1 and the numerical experiments in [5].

When the two neighboring cells have different permeability, there is no reason to expect continuity of velocity in the direction parallel to the face. Quite the contrary, if the ratio of the permeability is large one will get a proportionally large difference in the parallel component of the velocity in the two cells. In other words, the continuity condition (2.5) in [4] is incorrect. The paper claims that the permeability may vary strongly across cell faces, but it only shows numerical examples with homogeneous permeability. In a newer paper [8] this error is mentioned: "For problems with discontinuous coefficients, it is more natural to define additional discrete unknowns as tangential components of the gradient ∇p , rather than velocity \mathbf{u} . Fortunately, in practical applications, material interfaces are composed of moderately curved faces; therefore, we did not investigate other definitions of degrees of freedom." Unfortunately, this is not the case for the SBED model we shall consider in Section 5.2.3.

3.3 An alternative continuity condition

In this section we explore a way to adapt the curved mimetic method to work on heterogeneous isotropic permeability. Then we discuss if this approach can be extended to anisotropic permeability.

As mentioned, it was suggested in [8] to define the new unknowns by the gradient of the pressure, however the author of that paper have not explored this option. It would require quite some work to redefine the unknowns. Instead, we keep the unknowns and change the continuity condition.

We swap the false continuity condition with a condition for the unknowns on the following form:

$$v_{E_\beta}^s = \alpha v_{E_\gamma}^s, \quad s = 2, 3 \quad (3.45)$$

for some constant α , where $v_{E_\beta}^s$ and $v_{E_\gamma}^s$ are the velocity components associated with the face e . Here, E_β and E_γ are two cells who share a face e . Let \mathbf{a}_β^s and \mathbf{a}_γ^s , $s = 2, 3$ be the orthonormal vectors associated with the face e . Then

by definition $\mathbf{a}_\beta^s = -\mathbf{a}_\gamma^s$. Now we define the *face plane* as the plane spanned by the vectors \mathbf{a}^s , $s = 2, 3$. As the pressure is continuous, the projection of the pressure gradient onto the face plane must be continuous. Let

$$\Delta p_{E_j}^s = \nabla p \cdot \mathbf{a}_{E_j}^s, \quad \text{for } s = 2, 3 \text{ } j = \beta, \gamma. \quad (3.46)$$

Then $\Delta p_{E_\beta}^s = -\Delta p_{E_\gamma}^s$. Let the isotropic permeability in the two cells be $k_\beta \mathbf{I}$ and $k_\gamma \mathbf{I}$ respectively. We use the interpolation operator, Equation (3.17), to get an expression for the flux unknowns

$$\begin{aligned} v_{E_j}^s &= ((\vec{v})^I)_{E_j}^e \\ &= \int_e \vec{v}_{E_j} \cdot \mathbf{a}_j^s \, d\sigma. \end{aligned} \quad (3.47)$$

Inserting Darcy's law

$$\vec{v}_{E_j} = -k_j \mathbf{I} \nabla p \quad (3.48)$$

into Equation (3.47) we get

$$\begin{aligned} v_{E_j}^s &= \int_e -k_j (\nabla p \cdot \mathbf{a}_{E_j}^s) \, d\sigma \\ &= -k_j |e| \Delta p_{E_j}^s, \end{aligned} \quad (3.49)$$

for $s = 2, 3$ and $j = \beta, \gamma$. Here, \vec{v}_{E_β} and \vec{v}_{E_γ} are the exact velocity field on each side of the face e , and $v_{E_\beta}^s$ and $v_{E_\gamma}^s$ are flux unknowns associated with the local coordinate system of face e defined by the vectors \mathbf{a}^s , $s = 1, 2, 3$. Put together, this gives us

$$v_{E_\beta}^s = -\frac{k_\beta}{k_\gamma} v_{E_\gamma}^s, \quad s = 2, 3. \quad (3.50)$$

This continuity condition is exact for flat faces. How this will behave on strongly curved faces will be investigated in Section 5.3.

We note that this continuity condition will result in a non-symmetric hybrid formulation

$$\begin{bmatrix} \mathbf{B} & \mathbf{C} & \mathbf{D} \\ \mathbf{C}^T & \mathbf{0} & \mathbf{0} \\ \tilde{\mathbf{D}}^T & \mathbf{0} & \mathbf{0} \end{bmatrix} \begin{bmatrix} \mathbf{v} \\ -\mathbf{p} \\ \boldsymbol{\pi} \end{bmatrix} = \begin{bmatrix} \mathbf{0} \\ \mathbf{b} \\ \mathbf{0} \end{bmatrix}, \quad (3.51)$$

where \mathbf{D} and $\tilde{\mathbf{D}}$ have the non-zero elements at the same place. But while \mathbf{D} is the same as before, with only unit entries, $\tilde{\mathbf{D}}$ has the ratio between of the

permeabilities as entries. Throughout this thesis, this method will be called the *new curved mimetic method*.

The anisotropic case

If the above approach should work for anisotropic permeabilities, then Equation (3.49) would look

$$\begin{aligned} v_{E_j}^s &= \int_e -(\mathbf{K}_j \nabla p) \cdot \mathbf{a}_{E_j}^s \, d\sigma \\ &= -|e| (\nabla p)^T \mathbf{K}_j \mathbf{a}_{E_j}^s. \end{aligned} \quad (3.52)$$

If we assume ∇p to be continuous, and if we want a condition for the flux unknowns on the form of Equation (3.45), we need

$$\mathbf{K}_\beta = \alpha \mathbf{K}_\gamma, \quad (3.53)$$

which includes the isotropic case, and cases where the anisotropy rate is the same throughout the reservoir.

Proof: Let $\mathbf{x} = -|e| \nabla p$ and $\mathbf{b}_j^s = \mathbf{K}_j \mathbf{a}^s$. Equation (3.52) reads

$$v_{E_j}^s = \mathbf{x}^T \mathbf{b}_j^s \quad (3.54)$$

and Equation (3.45) can be written

$$\begin{aligned} 0 &= \mathbf{x}^T \mathbf{b}_\beta^s - \alpha \mathbf{x}^T \mathbf{b}_\gamma^s \\ &= \mathbf{x}^T (\mathbf{b}_\beta^s - \alpha \mathbf{b}_\gamma^s), \quad s = 2, 3. \end{aligned} \quad (3.55)$$

which can only be satisfied if $\mathbf{b}_\beta^s = \alpha \mathbf{b}_\gamma^s$, if it is to be valid for any \mathbf{x} .

Chapter 4

Implementation

In this chapter, we present the platform used for implementation. Then, the implementation of the curved mimetic method is discussed. We then discuss the implementation of boundary conditions for the mimetic method and suggest a way to implement boundary conditions also for strongly curved faces.

4.1 MRST

As a basis for implementation, we have used MATLAB Reservoir Simulation Toolbox (MRST)¹. MRST is an open-source MATLAB[®] toolbox developed by *SINTEF Applied Mathematics*. MRST contains routines for creating and manipulating very general grids, as well as numerical solvers for computing single and multi-phase flow, including TPFA, MPFA, multiscale methods and mimetic methods. MRST is developed as a platform to implement, verify and benchmark new numerical solvers. See [7] for an introduction to MRST.

4.2 The curved mimetic method

Implementation of the variables and matrices needed are based on approximations. Instead of using some surface formula for the faces, we do a triangulation of each face. Let N_e be the number of nodes defining a face e , and let e be divided into N_e triangles by connecting all corners of the face by the face mass center. See Figure 4.1 for an illustration. The matrix \mathbf{C} in Equation (3.37) is computed in the following way.

¹<http://www.sintef.no/MRST>

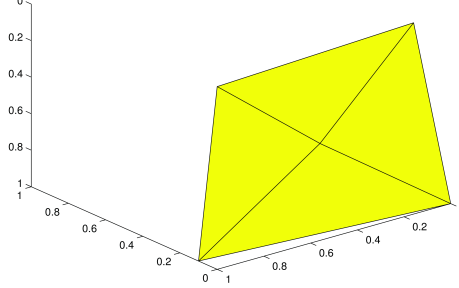


Figure 4.1: Triangulation of a curved face.

$$\begin{aligned}
\mathbf{c}_{E,i}^t &= \frac{1}{\beta_E^t} \int_{e_t} x_i \mathbf{a}_E^t \cdot \vec{\mathbf{n}}_E \, d\sigma \\
&\approx \frac{1}{\beta_E^t} \sum_{k=1}^{N_e} \int_{e_{t,k}} x_i \mathbf{a}_E^t \cdot \mathbf{n}^k \, d\sigma \\
&= \frac{1}{\beta_E^t} \sum_{k=1}^{N_e} \tilde{c}_{k,i} \mathbf{a}_E^t \cdot \mathbf{n}^k
\end{aligned} \tag{4.1}$$

where \mathbf{n}^k is the normal vector of the triangle $e_{t,k}$ and $\tilde{c}_{k,i}$ is the i -coordinate of the centroid of $e_{t,k}$

Similarly, the average normal vectors are calculated by summing up the normal vectors of the triangles.

We also need an implementation of the curvature constant in Equation (3.3). The approximation of the curvature constant σ for each face e is

$$\sigma = \max_{k=1,\dots,N_e} \left\| \frac{\mathbf{n}^k}{\|\mathbf{n}^k\|} - \frac{\tilde{\mathbf{n}}^e}{|e|} \right\| |e|^{-1/2} \tag{4.2}$$

4.3 Boundary conditions for the mimetic method

We will investigate the implementation of pressure and flux boundary conditions for the mimetic method, when set up on the form of Equation (4.3).

$$\begin{bmatrix} \mathbf{B} & \mathbf{C} & \mathbf{D} \\ \mathbf{C}^T & \mathbf{0} & \mathbf{0} \\ \mathbf{D}^T & \mathbf{0} & \mathbf{0} \end{bmatrix} \begin{bmatrix} \mathbf{v} \\ -\mathbf{p} \\ \boldsymbol{\pi} \end{bmatrix} = \begin{bmatrix} \mathbf{f} \\ \mathbf{g} \\ \mathbf{h} \end{bmatrix}, \quad (4.3)$$

For the flux case, we put the boundary flux values into the vector \mathbf{h} . The last line of Equation (4.3) reads $\mathbf{D}^T \mathbf{v} = \mathbf{h}$, and for all internal faces e , $h_e = 0$ and the corresponding line becomes $v_{E_1}^e + v_{E_2}^e = 0$. That is the mass conservation condition. For a boundary face e_b however, the matrix \mathbf{D} has only one unit entry, and the corresponding line becomes $v^{e_b} = h_{e_b}$.

The pressure boundary condition is implemented by removing the columns in \mathbf{D} corresponding to pressure boundary faces. The corresponding unknowns in $\boldsymbol{\pi}$ are also removed. Recall that the first line of Equation (4.3) reads $\mathbf{B}\mathbf{v} = \mathbf{C}\mathbf{p} - \mathbf{D}\boldsymbol{\pi} + \mathbf{f}$. Since the corresponding pressures are removed from $\mathbf{D}\boldsymbol{\pi}$ it is moved into the vector \mathbf{f} with a negative sign.

4.4 Boundary conditions for the curved mimetic method

In this section we discuss possible solutions on how to treat boundary conditions for curved boundary faces.

The mimetic approach

One possible solution is to increase the threshold level σ_* for the boundary faces, i.e., treating all boundary faces as moderately curved faces. In that case, the curved mimetic method and the mimetic method are equivalent for these boundary faces, and the implementation of boundary conditions is as discussed above. In our implementations, this is the standard way to treat boundary conditions.

Solutions with extra degrees of freedom on curved boundary faces

Another option would be to implement boundary conditions on strongly curved faces. We will now investigate how this can be done.

For the curved mimetic method the hybrid formulation reads:

$$\begin{bmatrix} \mathbf{B}_1 & \mathbf{0} & \mathbf{0} & \mathbf{C} & \mathbf{D}_1 & \mathbf{0} & \mathbf{0} \\ \mathbf{0} & \mathbf{B}_2 & \mathbf{0} & \mathbf{0} & \mathbf{0} & \mathbf{D}_2 & \mathbf{0} \\ \mathbf{0} & \mathbf{0} & \mathbf{B}_3 & \mathbf{0} & \mathbf{0} & \mathbf{0} & \mathbf{D}_3 \\ \mathbf{C}^T & \mathbf{0} & \mathbf{0} & \mathbf{0} & \mathbf{0} & \mathbf{0} & \mathbf{0} \\ \tilde{\mathbf{D}}_1^T & \mathbf{0} & \mathbf{0} & \mathbf{0} & \mathbf{0} & \mathbf{0} & \mathbf{0} \\ \mathbf{0} & \tilde{\mathbf{D}}_2^T & \mathbf{0} & \mathbf{0} & \mathbf{0} & \mathbf{0} & \mathbf{0} \\ \mathbf{0} & \mathbf{0} & \tilde{\mathbf{D}}_3^T & \mathbf{0} & \mathbf{0} & \mathbf{0} & \mathbf{0} \end{bmatrix} \begin{bmatrix} \mathbf{v}_1 \\ \mathbf{v}_2 \\ \mathbf{v}_3 \\ -\mathbf{p} \\ \pi_1 \\ \pi_2 \\ \pi_3 \end{bmatrix} = \begin{bmatrix} \mathbf{f}_1 \\ \mathbf{f}_2 \\ \mathbf{f}_3 \\ \mathbf{g} \\ \mathbf{h}_1 \\ \mathbf{h}_2 \\ \mathbf{h}_3 \end{bmatrix}. \quad (4.4)$$

We start by looking at the case of zero flux boundary, $\vec{v} \cdot \vec{n} = 0$ on $\partial\Omega_N$, where $\partial\Omega_N$ is the part of the boundary with zero flux and curved faces. The last three lines of Equation (4.4) reads $\tilde{\mathbf{D}}_1^T \mathbf{v}_1 = \mathbf{h}_1$, $\tilde{\mathbf{D}}_2^T \mathbf{v}_2 = \mathbf{h}_2$ and $\tilde{\mathbf{D}}_3^T \mathbf{v}_3 = \mathbf{h}_3$ respectively. The first of these corresponds to the velocity in the normal direction, and should be zero, i.e., letting the corresponding values of \mathbf{h}_1 equal zero. For the corresponding elements of $\tilde{\mathbf{D}}_i^T \mathbf{v}_i$ for $i = 2, 3$ there is no reason to constrain these unknowns to equal zero. Recall that the interpretation of the \mathbf{v}_2 and \mathbf{v}_3 unknowns is

$$\mathbf{v}_s = \int_e \vec{v} \cdot \mathbf{a}^{e,s} \, dS, \quad \text{for } s = 2, 3, \quad (4.5)$$

where \vec{v} is the velocity field. If the velocity field has a non-zero component in the direction parallel to the face, then the new unknowns are also non-zero.

Some condition on the new unknowns

One option would be to find some restriction or equation for the new unknowns on the boundary. However, the condition $\vec{v} \cdot \vec{n} = 0$ does not tell us what the parallel component of the velocity field should be, so we can not simply put in a numerical value in the \mathbf{h}_2 and \mathbf{h}_3 vectors. Options for restrictions or equations have not been investigated in this thesis.

Deletion of rows and columns

Another option is to delete the corresponding rows in the system, i.e., the corresponding columns of $\tilde{\mathbf{D}}_i$, $i = 2, 3$ and elements of \mathbf{h}_i , $i = 2, 3$.

Now the system matrix is no longer square, since we have more unknowns than equations. Since we do want a square system, we have chosen to delete the corresponding columns in \mathbf{D}_2 and \mathbf{D}_3 and elements of π_2 and π_3 . This changes the second and third line of Equation (4.4), which reads $\mathbf{B}_i \mathbf{v}_i = -\mathbf{D}_i \pi_i + \mathbf{f}_i$, $i = 2, 3$. We know from [8] that the unknowns π_i , $i = 2, 3$ can be interpreted as

$$\pi_E^{e,s} = \int_e p_E^e(\vec{n} \cdot \mathbf{a}_E^{e,s}) d\sigma. \quad (4.6)$$

Removing these unknowns is then equivalent to setting $\pi_E^{e,s} = 0$, and that can be interpreted as assuming $\vec{n} \cdot \mathbf{a}_E^{e,s} = 0$, i.e., assuming the face to be flat. Intuitively this could be just as bad as treating the face to be flat or moderately curved. This approach has been implemented, and numerical experiments to test this is done in Section 5.4.2. Throughout this thesis, this way to implement boundary conditions on curved boundary faces are called the *curved boundary condition*.

Note also that the deletion of rows in the \mathbf{D} matrices will result in a reduced Schur system of the same size as the case where the mimetic method is used on the boundary.

4.5 Grid refinement strategies

Later, we will be needing a mean of comparing the solutions by the different numerical solvers on models that do not yield an easy analytical solution. To this mean we use a grid refinement strategy. Since the examples used here have flat vertical faces, the grids are only refined in the x- and y-directions. The examples here are also Cartesian in the x- and y-direction, so choosing the x- and y-coordinates of the new nodes that define the division of the cells, is straight forward. The choice of z-coordinates do involve a choice. The first and simplest choice is to first refine in the x-direction using a linear interpolation of all coordinates, and then refine in the y-direction using a linear interpolation of the new points. However, this *smooth refinement* approach does not converge towards the interpretation of the geometry that is used in MRST. Recall that for curved faces, MRST interprets the geometry to be piece-wise flat following a triangulation.

We have also implemented a *piecewise flat refinement* method. In Figure 4.2 a curved face is plotted both as a triangulation and refined by the two different refinement strategies.

To be able to compare the face flux results, we sum the face flux multiplied by the unit normal vector for the refined faces that make up each original face, and then take the dot product with the average unit normal vector of the original face.

We note that the curvature constant σ for each face, as defined in Equation (3.4), will be approximately equal for all refined subfaces for the smooth approach. For the second approach, as shown in the middle plot of Figure 4.2,

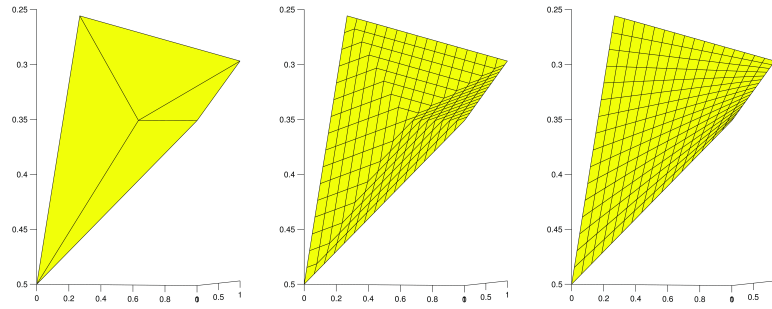


Figure 4.2: Plot of a curved face. Left: Triangulation that MRST use as interpretation of the face. Middle: Piecewise flat 16x16 refinement that follow this triangulation. Right: Smooth 16x16 refinement following a linear interpolation in x- and then y-direction.

the off-diagonal refined subfaces will be flat, and the refined subfaces on the diagonal will have an increasing curvature constant for finer refinements.

Chapter 5

Numerical experiments and results

In this chapter, the numerical experiments and results are presented. First, several test cases for the homogeneous case is presented. Then, two simple examples are run to verify that the naive continuity condition is invalid for the heterogeneous case. Then, the same two examples are run with the alternative continuity condition. We then explore more examples with the alternative continuity condition. Lastly, an example with a non-linear pressure field is presented.

5.1 The homogeneous case

In this section, we will look at some numerical experiments for the curved mimetic method on grids with homogeneous permeability. The first experiment is meant to motivate why we look into curved mimetic methods. Then we look at the efficiency for using the curved mimetic method on this example, and a similar example. Lastly we look at the efficiency for an SBED model. The aim of these experiments is to verify the accuracy of the curved mimetic method for the homogeneous case, and to investigate the efficiency of the curved mimetic method for these cases, i.e., we are looking at how much accuracy we can gain at what cost.

In these tests, we have chosen to measure the cost as the number of unknowns in the main system of equations that needs to be solved, and not the run-time of the solver. For the mimetic methods, this means the reduced Schur complement, and for the TPFA method the size of the system to be solved corresponds to the number of cells in the grid. This choice is made, because it is easy to measure, it is independent of the computer we run on,

and because the implementation might not be optimally implemented.

The Schur complement is a block-wise Gaussian elimination of Equation (2.7), see [7]. For both mimetic methods, solving the reduced Schur system is the major workload in the numerical method.

5.1.1 The simplest test

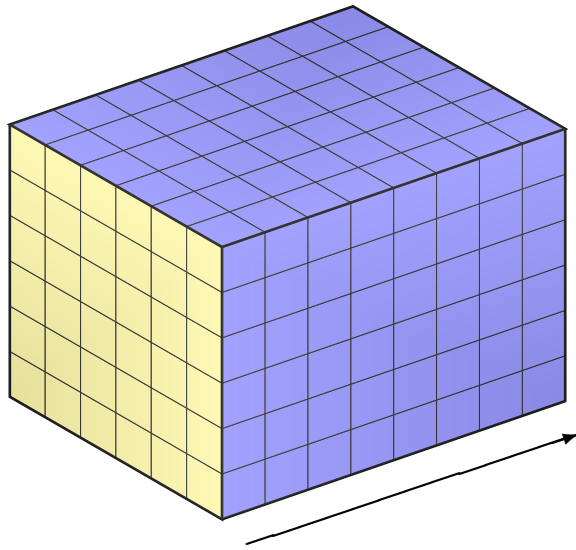
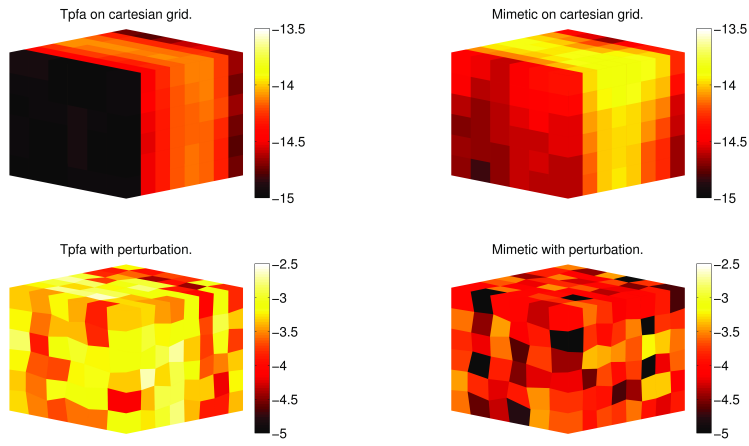
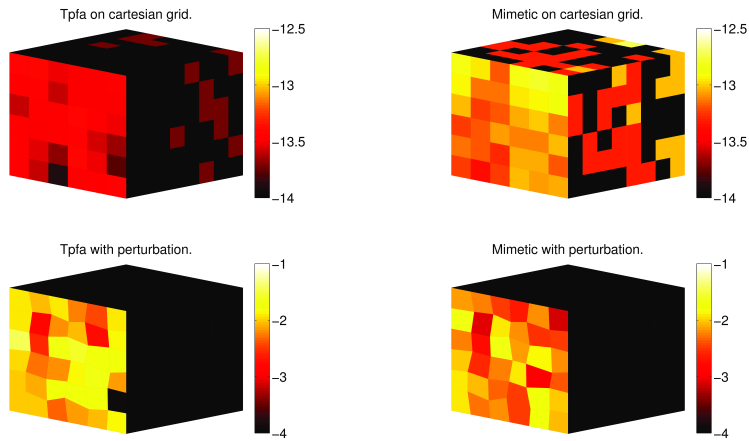


Figure 5.1: Global geometry of the test case. Prescribed Dirichlet boundaries (yellow) and homogeneous Neumann boundaries (blue). The analytical solution yields linear pressure drop and constant velocity field in the direction of the arrow.

We start with a simple example. The geometry of the example is a rectangular box. We use homogeneous permeability. The boundary conditions are Dirichlet boundary conditions for the pressure on two opposing sides, and homogeneous Neumann conditions on the other four sides. See Figure 5.1. The first grid on this example is a $8 \times 6 \times 6$ Cartesian grid. We have also compared this to a perturbed version of this grid. The perturbation is done by adding a random number in the region $(-\gamma, \gamma)$ to each of the coordinates to all internal nodes. For the nodes on the global boundary this perturbation is only done in the plane of the global face, and hence keeping the same global geometry.

Figure 5.2: \log_{10} plot of relative error in the pressure field.Figure 5.3: \log_{10} plot of relative error in the flux.

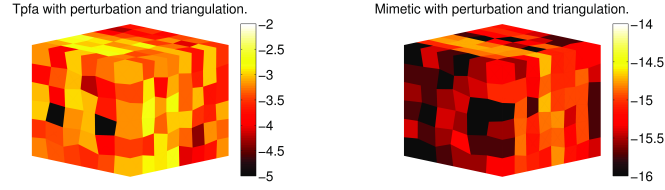


Figure 5.4: \log_{10} plot of relative error in the pressure field.

A comparison

To motivate why we want to look into mimetic methods for curved faces, we compare the Cartesian grid with a perturbed Cartesian (curvilinear) grid. Since the boundary and boundary conditions are the same, both grids yield an exact solution with linear pressure drop and constant velocity field. In Figure 5.2 we compare the TPFA and the mimetic method on a Cartesian grid, giving a point-wise absolute error relative to the max-norm of the exact solution of order 10^{-14} and 10^{-12} respectively. Then we perturb all internal nodes, and compare the same two methods. The perturbation is done using a random uniform distribution of $\gamma = 30$ cm. The reservoir in the plots have dimension $30 \times 10 \times 10$ meters, with the flow along the longest direction. This time the TPFA has an error of order 10^{-3} and the mimetic method an error of order 10^{-4} . In Figure 5.3 we see the same plot for the flux.

This example has $8 \times 6 \times 6 = 288$ cells. To compare the efficiency of these solvers, we compare the number of unknowns in the system. For the mimetic solver the size of the system (2.7) is $B : 1728 \times 1728, C : 1728 \times 288, D : 1728 \times 996$ giving a total of 3012 unknowns in the full system. After Schur complement the mimetic system is reduced to 924 unknowns. In comparison, the size of the TPFA system is 288. In other words, for this example, the difference between the TPFA method and the mimetic method is significant for the pressure and slight for the flux. And the advantage of the TPFA method is clearly its cost.

A first approach; triangulation

The perturbed grid in Figure 5.2 clearly contains cells having curved faces. One improvement on accuracy for the mimetic method is to split each face into four triangles, giving back flat faces, but increasing the number of faces in our grid. As we see in Figure 5.4 this gives the same accuracy as for the Cartesian grid for the mimetic method. However, since each face is split in four, we increasing the number of unknowns. As expected, the TPFA method

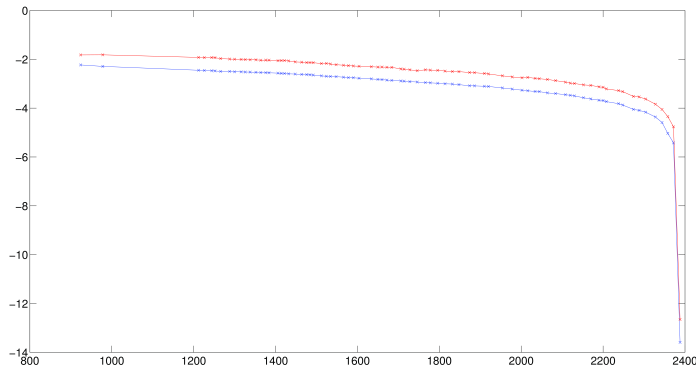


Figure 5.5: \log_{10} plot of relative error in L^2 norm in the flux (blue) and pressure (red) as a function of the number of unknowns in the Schur complement

does not improve accuracy by triangulation.

The size of the full mimetic system for the triangulated example is $B : 6912 \times 6912$, $C : 6912 \times 288$, $D : 6912 \times 3984$, giving a total of 11184 unknowns. After Schur complement this system reduces to 3696 unknowns versus 924 before triangulation. For the TPFA case the system still has 288 unknowns. Here, the cost of the mimetic method is very high, and hence we do not investigate triangulation any further. The TPFA system do not grow in size due to triangulation, but does not gain any accuracy either.

A test of the curved mimetic method

Now we want to look into the efficiency of the curved mimetic method. We start by running the same test as above; the rectangular grid with perturbed faces.

In Figure 5.5 we see the relative error plotted against the number of unknowns in the reduced Schur system. The plot is made by varying the curvature constant σ_* . Recall that σ_* is the threshold limit for which faces are treated as highly curved, i.e., given extra degrees of freedom. That is, all faces having a higher curvature than σ_* is treated as highly curved. By varying σ_* from over the value of the most curved face in the grid, to zero, i.e., treating all non-flat faces as highly curved, we gradually include more degrees of freedom. That way we get systems of increasing size and increasing accuracy.

In Figure 5.5 we see that there is no real gain in accuracy from just treating some of the faces as highly curved, i.e., in order to get a large

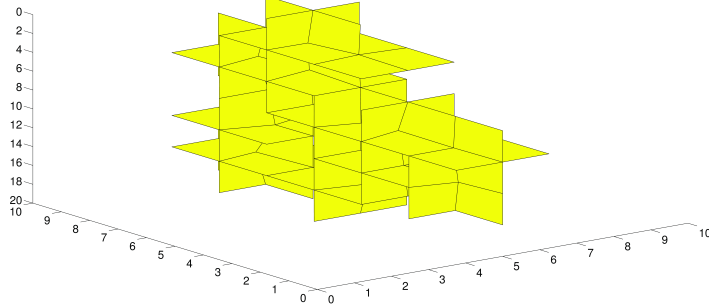


Figure 5.6: Plot of the highly curved faces.

improvement in accuracy, we need to treat all the faces as highly curved. We also see that when all the faces are treated as highly curved, we get a large improvement in accuracy. This improvement; the difference between the two rightmost data-points in Figure 5.5, is coming when going from treating just one curved face as moderately curved, to all curved faces as highly curved. It is reasonable that most of Figure 5.5 is a more or less straight line, since when all the faces have curvature of the same magnitude, we can expect them all to contribute equally to the error.

Variable curvature on the faces

To investigate if there are cases where one can find a significant improvement, without treating all the faces as highly curved, we look at the following case: We look at the same global geometry and boundary conditions as above. This time we have perturbed all nodes just slightly, giving a curvature constant of magnitude $\sigma_* \sim 10^{-4}$. And at one subsection across the flow direction, in the middle of the two Dirichlet boundaries, the faces are perturbed with a curvature constant of magnitude $\sigma_* \sim 0.05$. In Figure 5.6 one can see the positioning of the faces that have higher curvature.

As we can see from Figure 5.7 the gain in accuracy when just treating the faces with high curvature as highly curved we gain two orders of magnitude in the relative L^2 norm with the cost of going from approximately 900 to 1100 unknowns. The rest of Figure 5.7 looks similar to Figure 5.5. We also see a large gain in accuracy in the last step, 4 to 5 orders of magnitude. Again, this difference comes from only treating the face with the lowest curvature as moderately curved, and all other as highly curved versus all curved faces

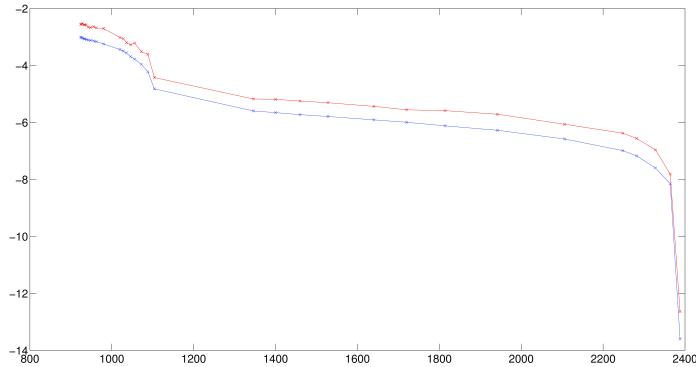


Figure 5.7: \log_{10} plot of relative error in L^2 norm in the flux (blue) and pressure (red) as a function of the number of unknowns in the Schur complement

as highly curved. In other words, for this model we see a significant gain in accuracy when treating just the worst faces with higher degrees of freedom.

In Table 5.1 we have listed the accuracy and number of unknowns for different models and methods. For model 1) and 2) in Table 5.1, the results are plotted point-wise in Figure 5.2 and 5.3 and Figure 5.4 respectively. For model 1) and 3) the results are plotted in Figure 5.5 and 5.7 respectively. These results show that for these simple examples, we are able to achieve machine precision by using the curved mimetic method. However the cost is high. For model 3) we have been able to achieve a significant gain in accuracy (relative error of order $\sim 10^{-5}$) by introducing just some extra degrees of freedom, i.e., just slightly higher cost. This is a promising result, however, these example grids are very simple. In the next subsection we run a test that are both bigger and more realistic.

5.1.2 SBED model

As this thesis intended to investigate the usefulness of the curved mimetic method for reservoir simulation, we run an SBED model. SBED models simulate the sedimentary structures with cell dimensions from millimeters to centimeters. Specific SBED grids can be made to represent what is found from core samples. From an SBED model one is able to calculate an approximation for the effective permeability for single and multi-phase flow as well as getting an estimate of the Representative Elementary Volume and thereby

	rel. L_2 -norm of pressure	rel. L_2 -norm of flux	# of unknowns	Model
TPFA	1.2e-3	7.5e-2	288	# 1
Mimetic	2.6e-4	8.6e-2	924	
Curved mimetic	2.3e-13	2.5e-14	2388	
TPFA	1.2e-3	1.5e-1	288	# 2
Mimetic	1.3e-15	4.3e-14	3696	
Mimetic	1.1e-4	5.8e-3	924	# 3
Curved mimetic	2.8e-3	9.8e-4	924	
Curved mimetic	3.7e-5	1.5e-5	1104	
Curved mimetic	2.3e-13	2.5e-14	2388	

Table 5.1: Relative L_2 -norm of the flux and pressure and number of unknowns for different methods and different models. The models are: 1) The model as in the bottom two plots in Figure 5.2. 2) Is the triangulated model, Figure 5.4. 3) Is the model with variably curved faces, from Figure 5.7.

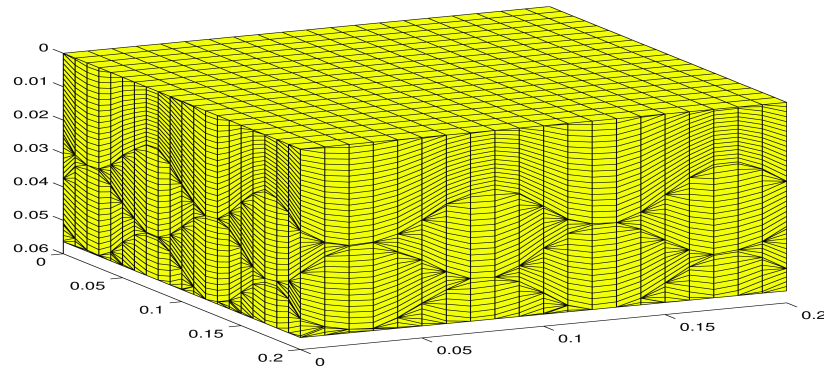


Figure 5.8: Plot of the SBED model. The physical size of this model is $20 \times 20 \times 5.64$ centimeters. It contains 18213 cells, of different shapes and sizes.

an optimal cell size for the reservoir grid. This SBED model¹ is a synthetic model, and the grid is plotted in Figure 5.8.

To verify that the curved mimetic method is accurate for homogeneous permeability, and to test the efficiency of the curved mimetic method on this grid, we have used the same boundary conditions as above; Dirichlet pressure conditions on two opposing sides, and homogeneous Neumann conditions on the other. Since we have homogeneous permeability and a linear pressure field, we have a simple analytical solution to compare with. The relative error in the L_2 -norm is plotted in Figure 5.9. The plot is made by running the simulation for different curvature constants σ_* . We see that when going from approximately 50 000 to 70 000 unknowns in the reduced Schur system, we gain one order of accuracy for the flux. And we see that when treating all faces as strongly curved, we gain machine precision with the curved mimetic method for the homogeneous case.

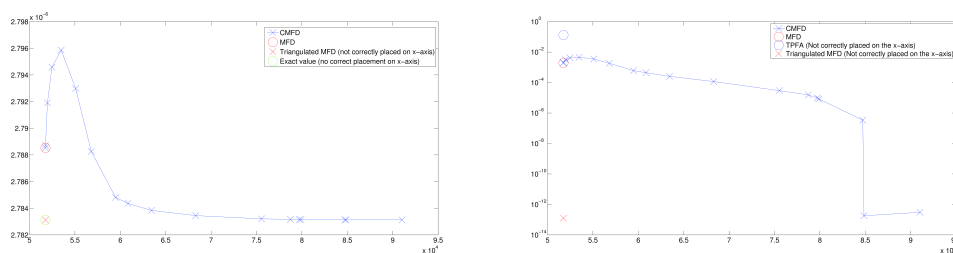


Figure 5.9: SBED model with homogeneous permeability. Total flux over the left Dirichlet boundary is plotted against the total number of unknowns in the Schur complement for the curved mimetic method. Values from the mimetic method is marked as a red circle and the mimetic method after a triangulation of the faces as a red cross. The left plot shows the values in $(\text{m}^3/\text{s}) = (\text{volume} / \text{time})$, and the right plot shows a \log_{10} of the relative error. The value for the TPFA method is also included in the right plot.

¹This Generic SBED model is copyright 2010 Statoil ASA, with Creative Commons license BY-SA 3.0. For more information about SBED, see: www.geomodeling.com

5.2 Tests of the naive continuity condition for the heterogeneous case

In this section we verify numerically that the naive continuity condition is incorrect for examples with discontinuous permeability over a strongly curved face. We first run a simple test with flat faces, where we force the curved mimetic method to use extra degrees of freedom on all internal faces. Then we run an example with curved faces.

5.2.1 A simple test case

As a first simple test, consider a $5 \times 1 \times 3$ Cartesian grid. We run this example because it is simple, and because the mimetic method yields the analytical solution. The permeability used is 1 milli Darcy in the top and bottom layers, and 50 milli Darcy in the middle layer. The grid and permeability is plotted in Figure 5.10. The boundary conditions are Dirichlet pressure on the left and right sides, and zero flux on the other four sides. This yields an exact solution of linear pressure drop, and a constant velocity field in each layer with a discontinuity across the layer of changing permeability. Since the faces are flat and the pressure field linear, the mimetic method will produce the exact solution to machine precision. Since all faces are planar, we have forced the curved mimetic method to treat all internal faces as strongly curved.

The flux for all faces is plotted in Figure 5.11 for the mimetic and the curved mimetic method. We see that the flux is significantly lower for the curved mimetic method in the high-permeable layer, and slightly higher in the low-permeable layers. This fits well with the enforced continuity of the velocity components parallel to the faces dividing cells of different permeability, and verifies that this continuity condition is incorrect.

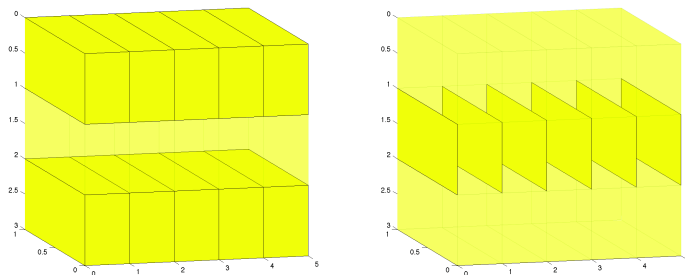


Figure 5.10: Plot of grid. Left: Cells with low permeability in dark yellow and cells with high permeability in transparent yellow. Right: Faces where the relative difference is larger than 5% in dark yellow.

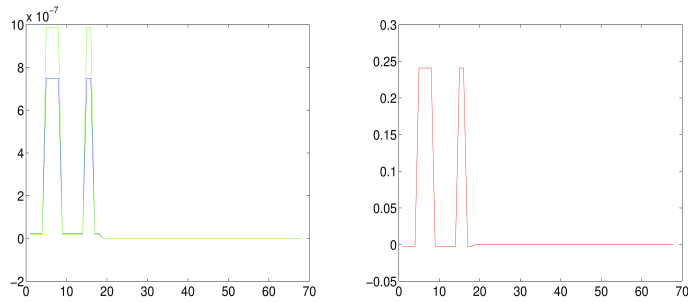


Figure 5.11: Plot of flux. Left: Flux across faces computed by mimetic method (green) and curved mimetic (blue). Right: Difference in flux by mimetic and curved mimetic relative to the max-norm of the mimetic solution.

To investigate the size of the error produced, we run the above test with varying ratio of permeability. We keep the permeability in the top and bottom layers constant at 1 milli Darcy, and vary the permeability in the middle. In Figure 5.12 we plot the maximum difference in the flux between the mimetic and the curved mimetic method, relative to the maximum of the mimetic method. We observe that the error is quickly converging to a stable limit as the ratio of permeability is increasing. The error is converging to approximately 25%.

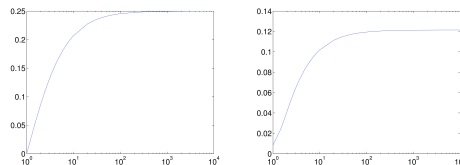


Figure 5.12: Semilogx plot of the maximum difference in the flux between the mimetic and curved mimetic method relative to the max-norm of the flux for the mimetic method versus the ratio of the permeability.

5.2.2 A test with curved faces

As the above test is done on flat faces, where we force the method to use full degrees of freedom on all internal faces, we now look at a grid with curved faces. We use a curvilinear grid, and the same boundary conditions and permeability as above; Dirichlet pressure on the left and right boundary, and zero flux elsewhere. Permeability is 1 milli Darcy in the top and bottom layers, and 50 milli Darcy in the middle. We now only use more degrees of freedom on curved faces. The grid and permeability is plotted in Figure 5.13

together with the faces where the difference between the mimetic and the curved mimetic method is large. This model does not have a simple analytical solution, but is compared to a solution using a refinement strategy as discussed in Section 4.5.

The grid is refined in x and y direction only, since all vertical faces are flat. We have refined each grid in 2x2, 4x4, 8x8 and 16x16 in the x and y directions. Assuming the 16x16 refined solution is the most accurate, we have plotted the L2-norm of the difference between the intermediate refinements and the 16x16 refinement solution relative to the L2 norm of the 16x16 refinement solution in Figure 5.15. We observe that the solution appears to converge as we refine. This supports our assumption that the 16x16 refinement is the most accurate.

We see that the same trend appears when the curved mimetic method is used as intended; on curved faces. The flux for each face is plotted in Figure 5.14. We observe that the difference in flux between the refined mimetic and the curved mimetic method in the faces perpendicular to the layer of changing permeability. In particular, the flux is significantly smaller in the cells with high permeability and slightly larger in the cells with low permeability. This fits well with the enforced continuity of the velocity components parallel to the faces dividing cells of different permeability. But since the velocity field is expected to be discontinuous here, this continuity condition is incorrect and the mimetic method produces a more accurate result.

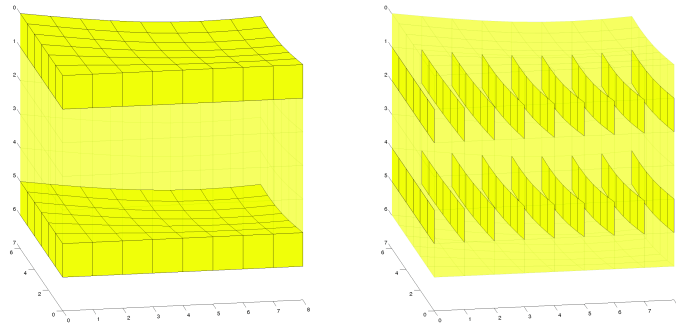


Figure 5.13: Plot of grid. Left: Cells with low permeability in dark yellow and cells with high permeability in transparent yellow. Right: Faces where the relative difference is larger than 5% in dark yellow.

As done for the example in Section 5.2.1 we have also for this example investigated the size of the error produced for varying ratio of permeability. Also for this example, we see a quick convergence, and this time the error converges to 12%, see Figure 5.16.

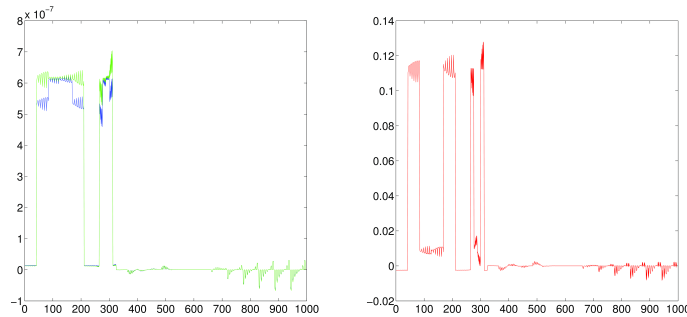


Figure 5.14: Plot of flux. Left: Flux across faces computed by refined mimetic method (green) and curved mimetic (blue). Right: Difference in flux by mimetic and curved mimetic relative to the max-norm of the refined mimetic solution.

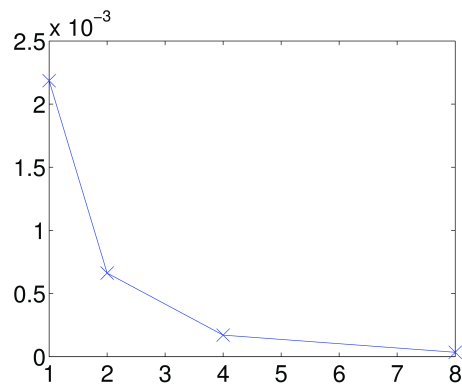


Figure 5.15: Convergence plot for the refinement strategy. Relative L2-norm of the difference to the solution for the 16x16 refinement on the y-axis. The x-axis shows the number of refinements in x- and y-direction, where 1 means no refinement.

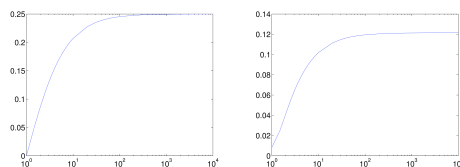


Figure 5.16: Semilogx plot of the maximum difference in the flux between the mimetic and curved mimetic method relative to the max-norm of the flux for the mimetic method versus the ratio of the permeability.

5.2.3 SBED model

In Section 5.1.2 we have tested the curved mimetic method on an example with homogeneous permeability and a realistic grid from reservoir simulation; an SBED grid. The grid is plotted in figure 5.8. In this subsection we will test the curved mimetic method with the naive continuity condition on this grid, with the same boundary conditions, but with realistic heterogeneous permeability. The ratio of the highest and lowest permeability is ~ 1000 .

This example is included to illustrate the effect of the naive continuity condition on a realistic example, and because it illustrates that the curved mimetic method do not behave as expected for heterogeneous permeability.

The total flux over the left pressure boundary is plotted against the number of unknowns in the Schur complement in Figure 5.17. We see that the difference between the methods increases in a linear fashion as more faces are treated with higher degrees of freedom. A comparison is run by triangulating all faces and running the mimetic method, yielding a similar solution as the mimetic method before triangulation. After triangulating, all faces are flat, and the mimetic method should then be exact for linear pressure fields. Even though this solution is not linear, we expect the solution to be a reasonable approximation. We note that the large drop in flux that appear when using the full curved mimetic method fits well with the above simple examples.

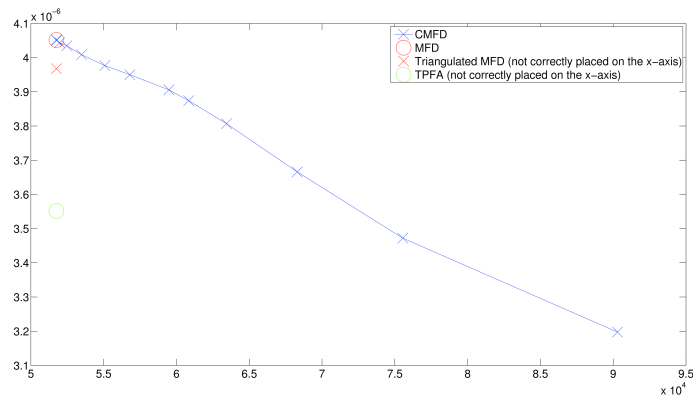


Figure 5.17: SBED model with heterogeneous permeability. Plot of total flux on the left Dirichlet boundary against number of unknowns in reduced Schur complement.

We note that for the SBED model, we do have curved faces at which the permeability is varying strongly across. The ratio of the permeability is plotted against the curvature of all internal faces in the SBED model in

Figure 5.18. Here we see that a large proportion of the faces are curved and have a ratio of permeability between 10 and 100.

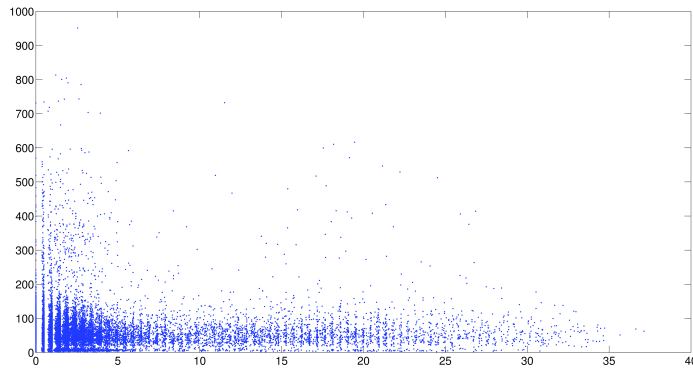


Figure 5.18: A dot is plotted for each internal face. On the y-axis is the ratio of permeability in the two neighboring cells. On the x-axis is the curvature constant σ from Equation (3.4).

5.3 Tests of the new curved mimetic method

In this section we run numerical experiments to test the new curved mimetic method. First, we run the same simple test cases as in Section 5.2. We then run a test case with curved faces for several choices of permeability, both isotropic and anisotropic.

5.3.1 A simple test case

The idea outlined in Section 3.3 has been implemented. First, we run the tests in Section 5.2.1 and 5.2.2. These tests are included to illustrate that the new curved mimetic method is correct for simple examples. The results are plotted in Figure 5.19 and 5.20. We observe that the new curved mimetic method gives an accurate result to machine precision for the first test. This is as expected, however on this example, the mimetic method is sufficient, and there is no gain in using the new curved mimetic method since the faces are flat.

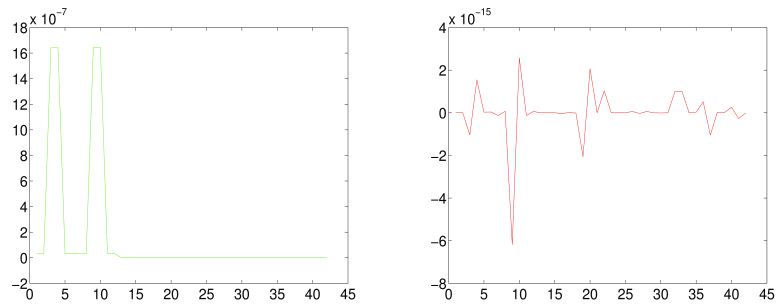


Figure 5.19: Same model as in Section 5.2.1. Plot of flux. Left: Flux across faces computed by mimetic method (green) and the new curved mimetic (blue). Right: Difference in flux by mimetic and the new curved mimetic relative to the max-norm of the mimetic solution.

The second test gives a relative difference of order 10^{-3} between the solutions obtained by the mimetic and the new curved mimetic methods. Here the faces are curved, and to determine which one is the most accurate, we compare the results using a refinement of the grid, as done in Section 5.2.2.

In Figure 5.21 we have plotted the point-wise difference between the flux solution in the original model and the refined model relative to the max-norm of the refined model. We observe that both models have an error of the same order ($\sim 1 \cdot 10^{-2}$), and that this error is larger than the difference between the two methods ($\sim 1 \cdot 10^{-3}$, see right plot in Figure 5.20). Also in relative L2 norm the difference to the refined model is similar for the two methods,

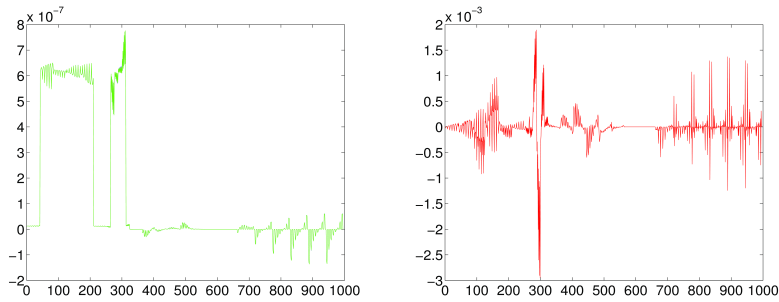


Figure 5.20: Same model as in Section 5.2.2. Plot of flux. Left: Flux across faces computed by mimetic method (green) and the new curved mimetic (blue). Right: Difference in flux by mimetic and the new curved mimetic relative to the max-norm of the mimetic solution.

they are $1.1 \cdot 10^{-2}$ for the new curved mimetic method, and $1.0 \cdot 10^{-2}$ for the mimetic method.

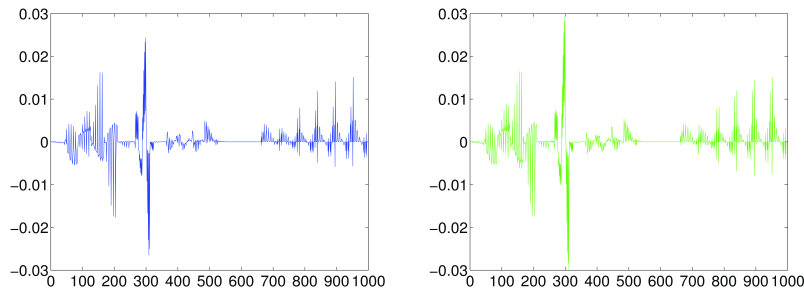


Figure 5.21: Point-wise difference to the refined model relative to the max-norm of the refined model in the mimetic method (left) and the new curved mimetic method (right).

So far the new curved mimetic method yield a similar result as the mimetic method, so more testing is needed. However if this result holds, i.e., that the two methods are equally accurate, then the new curved mimetic method is primarily of academic interest since it is more computationally demanding.

5.3.2 A test with curved faces

In this subsection we run a numerical experiment to investigate the difference between the mimetic and the new curved mimetic method. We test one grid with different permeabilities and geometrical ratios. This example is run to

investigate the accuracy of the new curved mimetic method and compare it to the accuracy of the mimetic method.

The model

The model we shall investigate, is a model where the boundary faces are flat, but with curved layers similar to those in Section 5.2.2. The grid is plotted in Figure 5.22. One motivation to run this model, is that it is similar to one common property in reservoir simulation. Typically long reservoirs that curve slightly in the horizontal directions. This is common, because oil and gas is found where it is trapped under a harder layer, typically concave. This means that the most realistic permeabilities for this model, is to have low permeability in the top and bottom layers, and higher permeabilities in the middle layers. We also test for different aspect ratios for the grid. The grid as plotted in Figure 5.22 has approximate cell dimensions of $1 \times 1 \times 1$ meters. In these examples we have used the smooth refinement method.

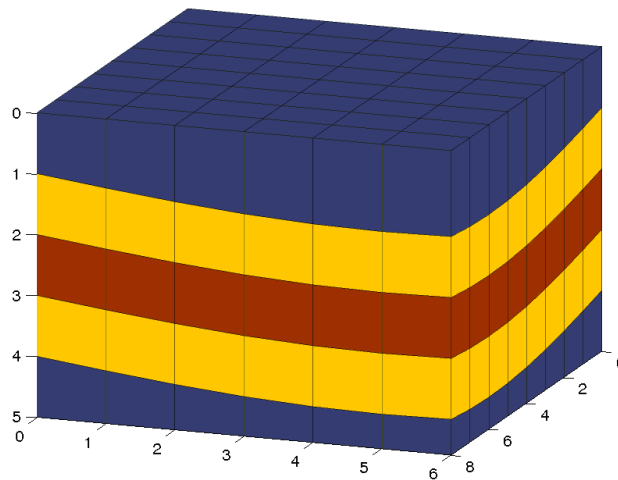


Figure 5.22: Plot of grid. The horizontal layers are given different permeabilities. We use the notation \mathbf{K}_1 for the blue, \mathbf{K}_2 for the yellow, and \mathbf{K}_3 for the red layers permeability respectively.

As boundary condition, we use Dirichlet pressure conditions on the left and right side, and zero flux conditions on the other four sides on all examples in this chapter.

Testing for different permeabilities.

We have run the test with different values for the permeability, different cell size ratios and compared to different methods run on the refined grid. In Table 5.3 the results is shown. The two first columns show $\|\mathbf{v}_{mim} - \mathbf{v}_{ref}\|_{L_2}/\|\mathbf{v}_{ref}\|_{L_2}$ and $\|\mathbf{v}_{cur} - \mathbf{v}_{ref}\|_{L_2}/\|\mathbf{v}_{ref}\|_{L_2}$ respectively. Where \mathbf{v}_{mim} is the solution from the mimetic method, \mathbf{v}_{cur} is the solution form the new curved mimetic method and \mathbf{v}_{ref} is the solution from the refined grid summed up to match the original gird.

In each block of rows, the same type of permeabilities are used, i.e., isotropic or anisotropic. The isotropic permeabilities are on the form $\mathbf{K}_i = k_i \mathbf{I}$. For the anisotropic case with anisotropy rate α , the permeability is $\mathbf{K}_i = \text{diag}(\alpha k_i, k_i, k_i)$, which satisfies Equation (3.53). Note that stretching the grid gives a similar behavior as an anisotropy; compare block 2 and 5 in Table 5.3.

The first block of rows is the case of isotropic permeability and close to square grid cells. For all ratios of permeability between the layers, we see that the two methods are approximately equally accurate. In fact the new curved mimetic method is slightly better for the homogeneous case, but this is also the least interesting case, since it has an analytical solution.

The second block of rows is the case where the grid is stretched. As mentioned, this is similar to block 5, where the permeability in the x-direction is reduced by a factor 100. In both cases, we see that the new curved mimetic method is more accurate for the homogenous case. When the top and bottom layers have low permeability, the two methods are approximately equal in accuracy. However, these cases are not typical in real life reservoirs. Quite the contrary, one would typically find that the permeability in the direction of the flow is higher than the vertical permeability. A more realistic case would be to run the example with grid ratios of order 10x10x1 to 100x100x1 and an anisotropy rate of 1 or greater. These cases are very similar to the uniform grid ratio (1x1x1).

The third and fourth block of rows is the case where the grid ratio is uniform, and an anisotropy rate of 100. As mentioned, anisotropies where the permeability is higher in the flow direction, is more common in reservoirs. In these cases, we see that the difference between the methods is small for the large differences in permeabilities, and for the homogeneous case. For the intermediate lines, colored in yellow, we note that when comparing to the mimetic method on the refined grid, the mimetic method is more accurate. And when comparing to the new curved mimetic method on the refined grid, the new curved mimetic method is more accurate. This suggests that when refining, the two methods converge to two different solutions for that set of

permeabilities. The same is not observed for the inverse anisotropy rate in the two bottom block of rows.

Table 5.2: Table of relative difference in the pressures for the examples of the first block of rows in Table 5.3. As a reference, the mimetic method on the refined grid is used.

Mimetic	Curved mimetic
9.86e-05	1.40e-04
9.17e-05	1.37e-04
5.21e-05	8.46e-05
3.83e-06	7.99e-06
2.56e-06	4.01e-08

In Table 5.2 the error in the pressure is estimated for the examples run in Table 5.3. The relative pressure difference is first calculated using the volume weighted norm. Then the mean of the 5 layers for each block of rows is plotted in Table 5.2. We observe that the accuracy in the pressure for the layers are more or less the same for all cases except for the last line, the homogeneous case, where the curved mimetic method is more accurate by two orders of magnitude.

Table 5.3: Table of the L2-norm of the difference between the methods and a refined reference solution relative to the L2-norm of the refined solution. We use either the mimetic method (*) or the new curved mimetic method (**) on the refined grid.

	Mimetic relative L2-norm	New curved mimetic relative L2-norm	\mathbf{K}_1 (mD)	\mathbf{K}_2 (mD)	\mathbf{K}_3 (mD)
Isotropic, cell ratio: 1x1x1 (*)	$2.2 \cdot 10^{-3}$	$3.1 \cdot 10^{-3}$	1000	500	1
	$2.0 \cdot 10^{-3}$	$2.8 \cdot 10^{-3}$	1000	900	1
	$1.0 \cdot 10^{-3}$	$1.5 \cdot 10^{-3}$	1000	900	300
	$6.6 \cdot 10^{-4}$	$1.6 \cdot 10^{-4}$	1000	950	900
	$6.9 \cdot 10^{-4}$	$1.0 \cdot 10^{-5}$	1000	1000	1000
Isotropic, cell ratio: 10x1x1 (*)	$2.4 \cdot 10^{-3}$	$2.4 \cdot 10^{-3}$	1000	500	1
	$2.7 \cdot 10^{-3}$	$2.7 \cdot 10^{-3}$	1000	900	1
	$3.0 \cdot 10^{-2}$	$1.8 \cdot 10^{-3}$	1000	900	300
	$5.8 \cdot 10^{-2}$	$9.1 \cdot 10^{-4}$	1000	950	900
	$6.0 \cdot 10^{-2}$	$9.1 \cdot 10^{-4}$	1000	1000	1000
Anisotropi rate 100, cell ratio: 1x1x1 (*)	$2.2 \cdot 10^{-3}$	$7.0 \cdot 10^{-3}$	1000	500	1
	$2.3 \cdot 10^{-3}$	$2.8 \cdot 10^{-2}$	1000	900	1
	$1.2 \cdot 10^{-3}$	$1.4 \cdot 10^{-2}$	1000	900	300
	$1.1 \cdot 10^{-4}$	$7.5 \cdot 10^{-4}$	1000	950	900
	$1.9 \cdot 10^{-5}$	$1.6 \cdot 10^{-6}$	1000	1000	1000
Anisotropi rate 100, cell ratio: 1x1x1 (**)	$7.3 \cdot 10^{-3}$	$1.8 \cdot 10^{-3}$	1000	500	1
	$3.1 \cdot 10^{-2}$	$2.0 \cdot 10^{-3}$	1000	900	1
	$1.5 \cdot 10^{-2}$	$1.0 \cdot 10^{-3}$	1000	900	300
	$6.3 \cdot 10^{-4}$	$8.1 \cdot 10^{-5}$	1000	950	900
	$1.9 \cdot 10^{-5}$	$1.6 \cdot 10^{-6}$	1000	1000	1000
Anisotropi rate 0.01, cell ratio: 1x1x1 (*)	$6.3 \cdot 10^{-3}$	$6.3 \cdot 10^{-3}$	1000	500	1
	$6.7 \cdot 10^{-3}$	$6.7 \cdot 10^{-3}$	1000	900	1
	$3.0 \cdot 10^{-2}$	$4.1 \cdot 10^{-3}$	1000	900	300
	$5.7 \cdot 10^{-2}$	$9.5 \cdot 10^{-4}$	1000	950	900
	$5.8 \cdot 10^{-2}$	$9.0 \cdot 10^{-4}$	1000	1000	1000
Anisotropi rate 0.01, cell ratio: 1x1x1 (**)	$6.3 \cdot 10^{-3}$	$6.3 \cdot 10^{-3}$	1000	500	1
	$6.7 \cdot 10^{-3}$	$6.7 \cdot 10^{-3}$	1000	900	1
	$3.0 \cdot 10^{-2}$	$4.1 \cdot 10^{-3}$	1000	900	300
	$5.8 \cdot 10^{-2}$	$3.6 \cdot 10^{-4}$	1000	950	900
	$5.9 \cdot 10^{-2}$	$1.6 \cdot 10^{-6}$	1000	1000	1000

5.4 Curved mimetic method on strongly curved boundary faces

In this section we test the *curved boundary condition* suggested in Section 4.4. First, we run a test to verify that the method achieves a correct result on a simple example. Then we run an example similar to the one in Section 5.3.2.

5.4.1 A simple test

To test if the boundary condition is correct, we run a simple example. A reservoir shaped as a cylinder. The grid is plotted in Figure 5.23. We have chosen this example because it has curved boundary faces and yield an analytical solution. We use pressure boundary conditions on the two ends of the cylinder, and zero flux on the rest of the boundary. With a constant permeability this yields an analytical solution of linear pressure drop and constant velocity field.

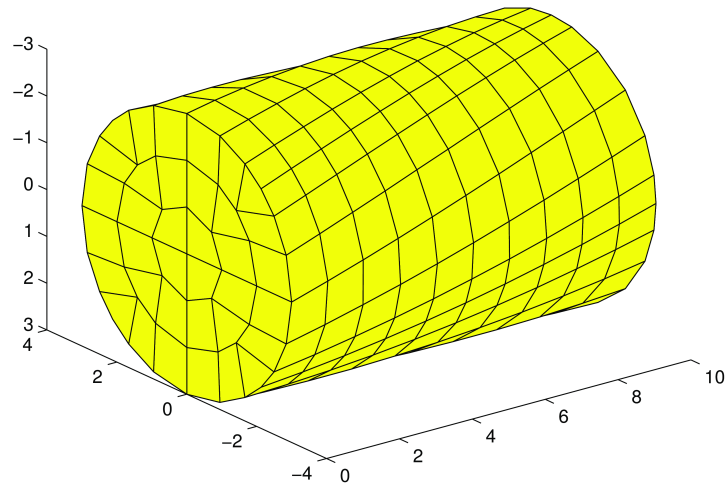


Figure 5.23: Plot of grid.

As we see from Table 5.4, the curved boundary condition yields a similar result as the mimetic boundary condition, i.e., treating curved boundary faces as moderately curved. In other words the curved boundary condition yield a reasonable result for this example, but has no benefit since the accuracy is of the same order but slightly worse than the standard approach.

Table 5.4: Table of relative error in flux and pressure for different numerical methods on the boundary.

	Flux rel. L2-norm	Pressure rel. L2-norm
Mimetic	$1.03 \cdot 10^{-3}$	$5.60 \cdot 10^{-6}$
Curved mimetic	$7.33 \cdot 10^{-3}$	$8.15 \cdot 10^{-5}$
Curved mimetic with new BC	$7.41 \cdot 10^{-3}$	$8.12 \cdot 10^{-5}$

5.4.2 A test with curved faces

In this subsection we run a test case with variable permeability to see if we can find a case where the curved boundary condition will give a more accurate result than the mimetic approach. We use a similar example as in Section 5.3.2, a reservoir with curved layers in the horizontal direction. It coincides with the middle three layers of the example from Section 5.3.2. The grid is plotted in Figure 5.24.

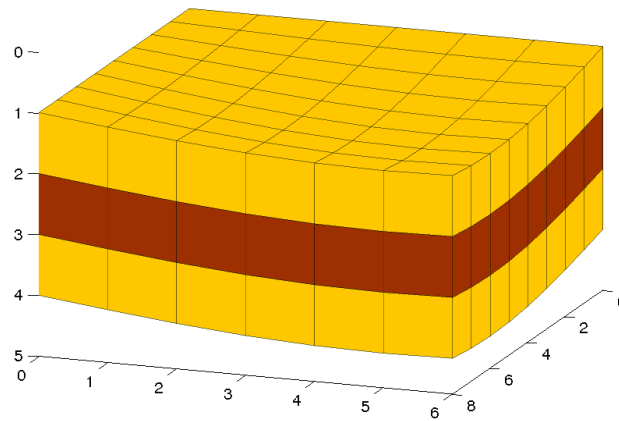


Figure 5.24: Plot of grid. The horizontal layers are given different permeabilities. We use the notation \mathbf{K}_1 for the red and \mathbf{K}_2 for the yellow layers permeability respectively.

As a reference solution, two strategies have been used. First, a refinement strategy on the grid and second to use the grid as plotted in Figure 5.22 with a very low value of permeability for the blue layers, simulating a close to zero flux boundary condition.

Table 5.5: Table of the L2-norm of the difference between the methods and a reference solution relative to the L2-norm of the reference solution. As a reference solution we use either the mimetic method with extra layers with very low permeability (*) or a refined grid and the mimetic method (**).

	New curved mimetic		Mimetic	\mathbf{K}_1	\mathbf{K}_2	\mathbf{K}_3
	curved BC	mimetic BC				
	rel. L2-norm	rel. L2-norm	rel. L2-norm	(mD)	(mD)	(mD)
Isotropic, cell ratio: 1x1x1 (*)	$4.5 \cdot 10^{-5}$	$4.5 \cdot 10^{-5}$	$1.7 \cdot 10^{-7}$	1000	10	0.001
	$9.5 \cdot 10^{-4}$	$9.5 \cdot 10^{-4}$	$1.6 \cdot 10^{-7}$	1000	300	0.001
	$1.3 \cdot 10^{-3}$	$1.3 \cdot 10^{-3}$	$1.4 \cdot 10^{-7}$	1000	500	0.001
	$1.5 \cdot 10^{-3}$	$1.5 \cdot 10^{-3}$	$1.0 \cdot 10^{-7}$	1000	900	0.001
	$1.3 \cdot 10^{-3}$	$1.6 \cdot 10^{-3}$	$9.8 \cdot 10^{-8}$	1000	1000	0.001
Isotropic, cell ratio: 10x1x1 (*)	$1.7 \cdot 10^{-3}$	$1.7 \cdot 10^{-3}$	$1.4 \cdot 10^{-7}$	1000	10	0.001
	$4.3 \cdot 10^{-2}$	$4.3 \cdot 10^{-2}$	$1.3 \cdot 10^{-7}$	1000	300	0.001
	$6.2 \cdot 10^{-2}$	$6.2 \cdot 10^{-2}$	$1.1 \cdot 10^{-7}$	1000	500	0.001
	$7.9 \cdot 10^{-2}$	$7.9 \cdot 10^{-2}$	$8.4 \cdot 10^{-8}$	1000	900	0.001
	$8.1 \cdot 10^{-2}$	$8.1 \cdot 10^{-2}$	$7.8 \cdot 10^{-8}$	1000	1000	0.001
Anisotropi rate 100, cell ratio: 1x1x1 (*)	$1.3 \cdot 10^{-1}$	$1.3 \cdot 10^{-1}$	$3.4 \cdot 10^{-7}$	1000	10	0.001
	$2.2 \cdot 10^{-2}$	$2.2 \cdot 10^{-2}$	$4.1 \cdot 10^{-7}$	1000	300	0.001
	$7.7 \cdot 10^{-3}$	$7.7 \cdot 10^{-3}$	$4.0 \cdot 10^{-7}$	1000	500	0.001
	$2.6 \cdot 10^{-2}$	$2.6 \cdot 10^{-2}$	$3.5 \cdot 10^{-7}$	1000	900	0.001
	$3.8 \cdot 10^{-2}$	$2.8 \cdot 10^{-2}$	$3.4 \cdot 10^{-7}$	1000	1000	0.001
Anisotropi rate 100, cell ratio: 1x1x1 (**)	$1.3 \cdot 10^{-1}$	$1.3 \cdot 10^{-1}$	$2.7 \cdot 10^{-3}$	1000	10	n/a
	$2.2 \cdot 10^{-2}$	$2.2 \cdot 10^{-2}$	$2.2 \cdot 10^{-3}$	1000	300	n/a
	$9.0 \cdot 10^{-3}$	$9.0 \cdot 10^{-3}$	$2.2 \cdot 10^{-2}$	1000	500	n/a
	$2.5 \cdot 10^{-2}$	$2.5 \cdot 10^{-2}$	$2.3 \cdot 10^{-3}$	1000	900	n/a
	$2.8 \cdot 10^{-2}$	$2.8 \cdot 10^{-2}$	$2.3 \cdot 10^{-3}$	1000	1000	n/a
Anisotropi rate 0.01, cell ratio: 1x1x1 (*)	$1.6 \cdot 10^{-3}$	$1.6 \cdot 10^{-3}$	$1.3 \cdot 10^{-7}$	1000	10	0.001
	$4.1 \cdot 10^{-2}$	$4.1 \cdot 10^{-2}$	$1.2 \cdot 10^{-7}$	1000	300	0.001
	$5.9 \cdot 10^{-2}$	$5.9 \cdot 10^{-2}$	$1.1 \cdot 10^{-7}$	1000	500	0.001
	$7.5 \cdot 10^{-2}$	$7.5 \cdot 10^{-2}$	$8.2 \cdot 10^{-8}$	1000	900	0.001
	$7.7 \cdot 10^{-2}$	$7.7 \cdot 10^{-2}$	$7.7 \cdot 10^{-8}$	1000	1000	0.001
Anisotropi rate 0.01, cell ratio: 1x1x1 (**)	$1.6 \cdot 10^{-3}$	$1.6 \cdot 10^{-3}$	$2.8 \cdot 10^{-4}$	1000	10	n/a
	$4.1 \cdot 10^{-2}$	$4.1 \cdot 10^{-2}$	$5.0 \cdot 10^{-3}$	1000	300	n/a
	$5.9 \cdot 10^{-2}$	$5.9 \cdot 10^{-2}$	$6.3 \cdot 10^{-3}$	1000	500	n/a
	$7.5 \cdot 10^{-2}$	$7.5 \cdot 10^{-2}$	$6.7 \cdot 10^{-3}$	1000	900	n/a
	$7.7 \cdot 10^{-2}$	$7.7 \cdot 10^{-2}$	$6.5 \cdot 10^{-3}$	1000	1000	n/a

From Table 5.5 we see that the curved boundary condition does not gain any accuracy to the version where the mimetic method is used on the boundary. This confirms our assumption in Section 4.4 that it involves the assumption of a flat boundary face, and hence no accuracy is gained. It is also worth noticing that for all cases, the standard mimetic method is better. What can not be seen from the table, is that the relative difference in L2-norm between the two boundary strategies, were of order $\sim 10^{-3}$ for all examples.

5.5 An example with wells

In this section we will run an example with wells. The example is based on a 2D analytical solution, and is extended to 3D. This test is run to investigate the behavior of the curved mimetic method on solutions with non-linear pressure field and non-constant velocity field. Since the mimetic and the curved mimetic methods only are exact for linear pressure fields, it is interesting to test and compare their behavior when this criteria is not fulfilled. Especially since all practical applications involve non-linear pressure fields. Throughout this section, homogeneous permeability is used.

5.5.1 The model

In an infinitely large 2D reservoir, with a finite number of point wells q_i , $i = 1, \dots, N$, the following solution for the pressure is exact [9].

$$p(x, y) = \sum_i \frac{q_i}{2\pi K/\mu} \ln(\sqrt{(x - x_i)^2 + (y - y_i)^2}). \quad (5.1)$$

To extend this to three dimensions, we place point sources / sinks in a finite number of columns of cells, and evaluate the pressure in only one layer of cells in the middle of the reservoir. The analytical pressure solution is used on the boundary that coincide with the 2D boundary, and zero flux boundary condition is used on the top and bottom boundary.

5.5.2 A first test with flat faces

As a first test, we run a $49 \times 49 \times 5$ Cartesian grid with three columns of point sources. This test is run to ensure that the extension to three space dimensions is reasonable. A plot of the cells with the columns of point sources / sinks are plotted in Figure 5.25. We have also run the curved mimetic method on this grid to investigate if it behaves differently than the mimetic method for this example. Since this example has flat faces, we force the method to apply extra degrees of freedom on all internal faces.

In Figure 5.26, the resulting pressure in the cells in the middle layer is plotted as a scatter plot against the approximate analytical solution. If the method is exact, this plot should be a straight line. A point-wise difference between the methods relative to the approximate analytical solution is shown in Figure 5.27. We note that the mimetic method differ from the approximate analytical solution of order 1% point-wise relative to the max-norm of the approximate analytical solution, and that the error is small away from the wells.

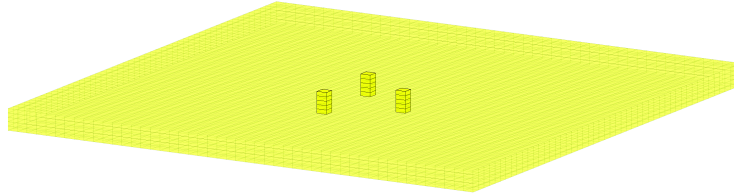


Figure 5.25: Plot of the grid. The cells that contain point sources / sinks are plotted in dark yellow. Two of the columns have a source rate of 1, and the third a source rate of -2 (i.e. a sink).

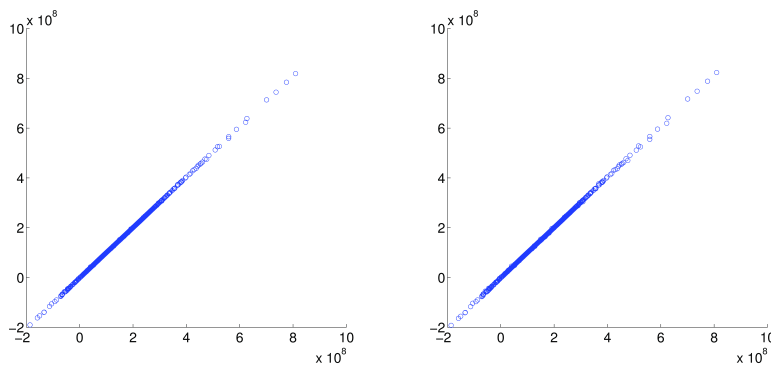


Figure 5.26: Scatter plot of the pressure solution against the approximate analytical solution for the mid section of the grid. Left: The mimetic method. Right: The curved mimetic method.

In Figure 5.28 we have plotted the point-wise difference between the two methods relative to the max-norm of the mimetic solution. As we can see from this figure, the relative point-wise difference between the pressure solution of the two methods are of order $\sim 10^{-3}$, which is 2 orders of magnitude smaller than the respective methods' relative difference to the approximate analytical solution. In Table 5.6 the relative L2-norm of the pressure is shown. Also here, we see that the two methods give approximately the same result relative to the approximate analytical solution. And that the relative difference between the two methods are less, but not a full order smaller.

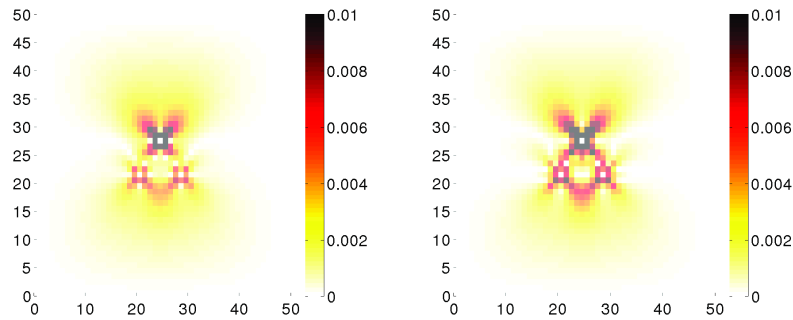


Figure 5.27: Plot of the relative difference in pressure between the approximate analytical solution and the mimetic solution for the mid-section. Left: Mimetic method. Right: Curved mimetic method.

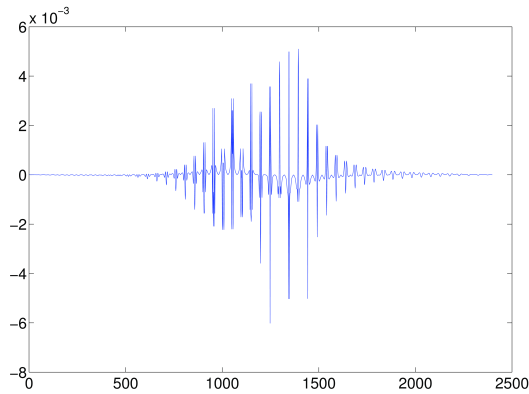


Figure 5.28: Plot of cell wise relative difference in pressure for the cells in the mid-section. The plot shows the the difference in pressures between the solution from the mimetic and the curved mimetic method relative to the max-norm of the solution from the mimetic method.

Table 5.6: Table of relative difference in the pressures.

Methods	Relative L2-norm
Mimetic vs approx. analytical	7.14e-3
Curved mimetic vs approx. analytical	8.68e-3
Mimetic vs curved mimetic	2.50e-3

5.5.3 A test with curved faces

Since the above example are run on a grid with flat faces, we will now introduce an example with curved faces. The grid is plotted in Figure 5.29.

We observe from Table 5.7 that the relative L2-norm of the difference in pressure between the mimetic and the curved mimetic method is 3 orders of magnitude smaller than the difference between either of the two method and the approximate analytical solution. In other words, there is little difference between the two methods in this example.

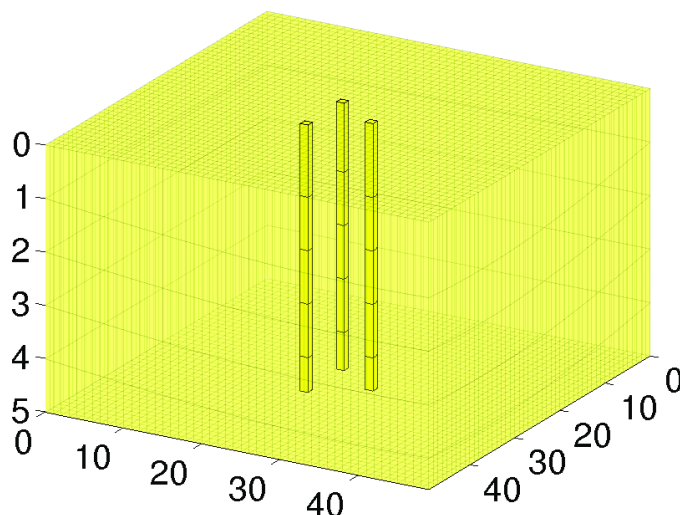


Figure 5.29: Plot of the grid. The cells that contain point sources / sinks are plotted in dark yellow. Two of the columns have a source rate of 1, and the third a source rate of -2 (i.e. a sink). Note that the axis in this plot is scaled differently in the z-direction.

Table 5.7: Table of relative difference in the pressures for the well example with curved faces.

Methods	Relative L2-norm
Mimetic vs approx. analytical	1.01e-2
Curved mimetic vs approx. analytical	1.02e-2
Mimetic vs curved mimetic	7.65e-5

Scatter plots of the pressure against the approximate analytical solution is shown in Figure 5.30. In Figure 5.31 the point-wise relative difference to the approximate analytical solution is shown. From these two plots, we see that the mimetic and the curved mimetic method yield a similar result. And that they both differ from the approximate analytical solution point-wise of order $\sim 1\%$

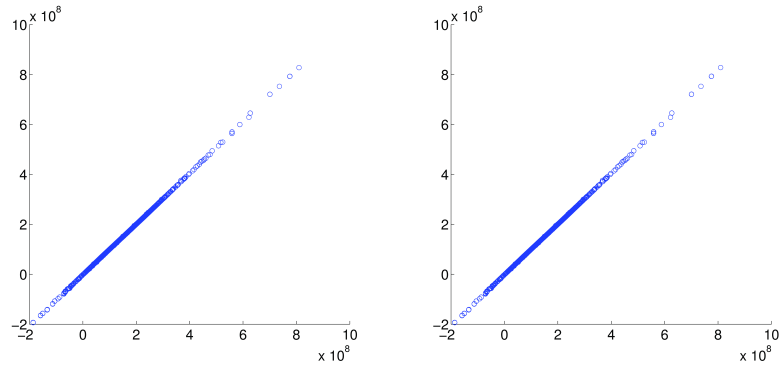


Figure 5.30: Scatter plot of the pressure solution against the approximate analytical solution for the mid section of the grid with curved faces. Left: The mimetic method. Right: The curved mimetic method.

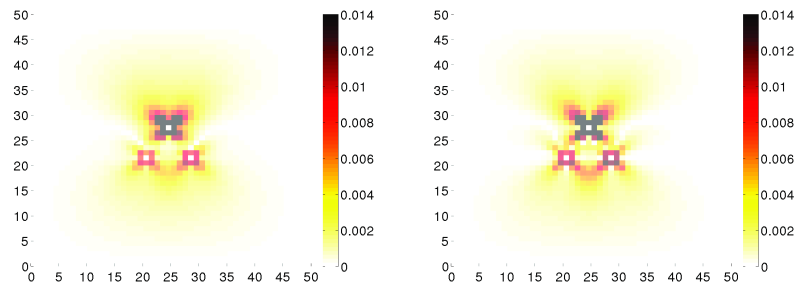


Figure 5.31: Plot of the relative difference in pressure between the approximate analytical solution and the mimetic solution for the mid-section of the grid with curved faces. Left: Mimetic method. Right: Curved mimetic method.

5.5.4 A test on a perturbed grid

We have now tested one example with curved faces. Since we want to say something about the accuracy of the method, and since we do this by running experiments, then the more experiments we run, the more confidence we can have in our findings. Therefore we run another example with curved faces. The grid is plotted in Figure 5.32. This is the same grid as in Section 5.5.2 with the same columns of point sources / sinks as above but with a perturbation of the inner nodes.

Scatter plots of the pressure is shown in Figure 5.33. We see that both the mimetic and the curved mimetic method results in a reasonable equally good result. Relative L2-norm for the pressure solutions are shown in Table 5.8. Again we see that there is little difference between the two methods, and that

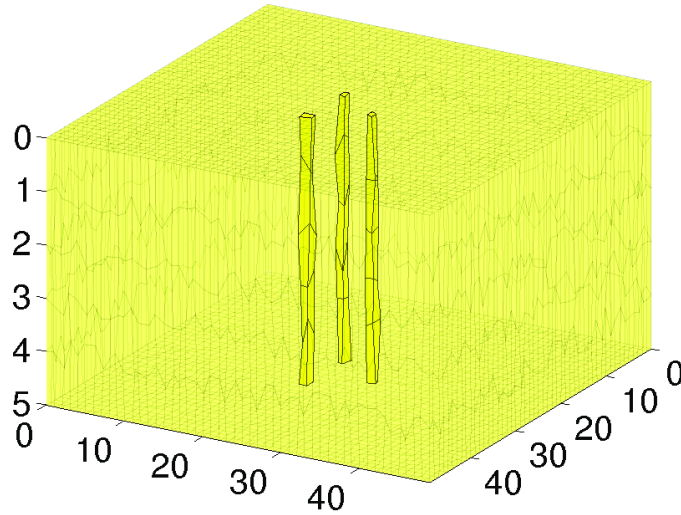


Figure 5.32: Plot of the grid. The cells that contain point sources / sinks are plotted in dark yellow. Two of the columns have a source rate of 1, and the third a source rate of -2 (i.e. a sink). Note that the axis in this plot is scaled differently in the z-direction.

the relative difference between them is one order smaller than their respective accuracy to the approximate analytical solution. This supports our findings that the curved mimetic method has little gain in accuracy compared to the mimetic method.

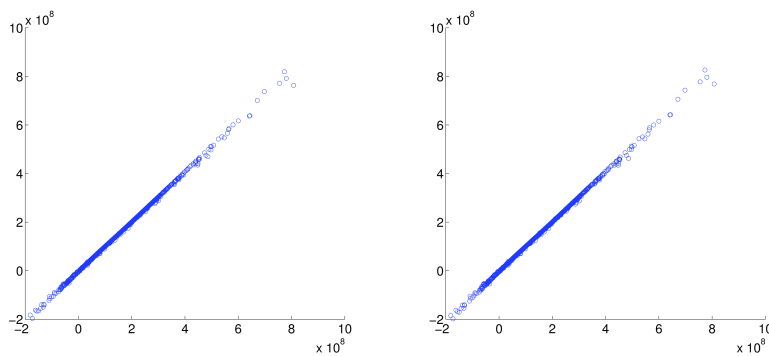


Figure 5.33: Scatter plot of the pressure solution against the approximate analytical solution for the mid section of the grid. Left: The mimetic method. Right: The curved mimetic method.

Table 5.8: Table of relative difference in the pressures for the well example with perturbed grid nodes.

Methods	Relative L2-norm
Mimetic vs approx. analytical	1.73e-2
Curved mimetic vs approx. analytical	1.86e-2
Mimetic vs curved mimetic	2.98e-3

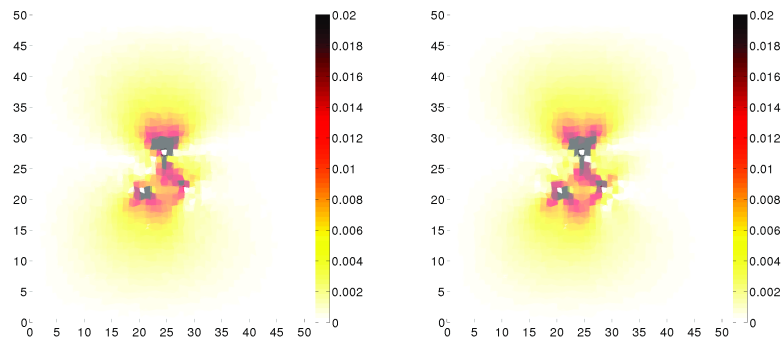


Figure 5.34: Plot of the relative difference in pressure between the approximate analytical solution and the mimetic solution for the mid-section of the grid with perturbed nodes. Left: Mimetic method. Right: Curved mimetic method.

Chapter 6

Conclusion and further work

In this chapter, we sum up the conclusions and present ideas for further work.

Conclusion

In this thesis, we have implemented the curved mimetic method, and investigated its performance with an emphasis on applications in reservoir simulation. The continuity condition suggested in [4, 5] is discussed. For the special case of homogeneous permeability, the curved mimetic method and its continuity condition is correct. However, for grids which has a discontinuity in the permeability over a curved face, the continuity condition suggested in [4, 5] is incorrect. And unfortunately, in reservoir simulation there are no or few applications with homogeneous permeability.

We have suggested and implemented an alternative continuity condition, and investigated the performance of this new curved mimetic method. The findings were that this new curved mimetic method had a very similar but slightly worse accuracy than the mimetic method. We also know that the (new) curved mimetic method introduces new unknowns, and hence is more computationally expensive than the mimetic method. The cost of the new curved mimetic method is discussed for the homogeneous case, and the number of unknowns will be the same for the new curved mimetic method for the heterogeneous case.

For the homogeneous case, the curved mimetic method is more accurate than the mimetic method. And cases where the gain in accuracy is significant for only a slight increase in cost is found. However, homogeneous cases is as mentioned not common in realistic examples.

The curved mimetic method is also tested on an example with a non-linear pressure field. Also for this case, the difference between the mimetic

and the curved mimetic method was small. And since the curved mimetic method is more computationally expensive, it is not recommended to be used in practical applications for this case either.

In other words, for realistic examples, the new curved mimetic method is significantly more expensive and has slightly lower accuracy, and based on the examples run in this thesis we conclude that the method is primarily of academic interest.

Further work

Since the conclusions about the accuracy of the new curved mimetic method is based on numerical examples, one could always wish for more test cases to see if it is possible to find cases where the new curved mimetic method is more accurate. However, the examples run in this thesis do show a clear indication that this method has no gain in accuracy compared to the mimetic method.

A more interesting topic for further work, would be to redefine the unknowns to be unknowns in the pressure gradient rather than the flux as suggested in [8]. However, we do not know how or if this can be done.

Finding other possibilities for continuity conditions for the new unknowns is also an area where it could be possible to improve the method.

Bibliography

- [1] J. E. Aarnes, T. Gimse, and K.-A. Lie. An introduction to the numerics of flow in porous media using Matlab. In *Geometric modelling, numerical simulation, and optimization: applied mathematics at SINTEF*, pages 265–306. Springer, Berlin, 2007.
- [2] I. Aavastmark. Bevarelsesmetoder for elliptiske differensialligninger. Universitetet i Bergen, 2007. <http://folk.uib.no/fciia/elliptisk.pdf>.
- [3] F. Brezzi, K. Lipnikov, and M. Shashkov. Convergence of the mimetic finite difference method for diffusion problems on polyhedral meshes. *SIAM J. Numer. Anal.*, 43(5):1872–1896 (electronic), 2005.
- [4] F. Brezzi, K. Lipnikov, and M. Shashkov. Convergence of mimetic finite difference method for diffusion problems on polyhedral meshes with curved faces. *Math. Models Methods Appl. Sci.*, 16(2):275–297, 2006.
- [5] F. Brezzi, K. Lipnikov, M. Shashkov, and V. Simoncini. A new discretization methodology for diffusion problems on generalized polyhedral meshes. *Comput. Methods Appl. Mech. Engrg.*, 196(37-40):3682–3692, 2007.
- [6] F. Brezzi, K. Lipnikov, and V. Simoncini. A family of mimetic finite difference methods on polygonal and polyhedral meshes. *Math. Models Methods Appl. Sci.*, 15(10):1533–1551, 2005.
- [7] K.-A. Lie, S. Krogstad, I. S. Ligaarden, J. R. Natvig, H. M. Nilsen, and B. Skaflestad. Open source matlab implementation of consistent discretisations on complex grids. *Comput. Geosci.*, 16(2):297–322, 2012.
- [8] K. Lipnikov and G. Manzini. Benchmark 3d: Mimetic finite difference method for generalized polyhedral meshes. In J. Fořt, J. Fürst, J. Halama, R. Herbin, and F. Hubert, editors, *Finite Volumes for Complex*

Applications VI Problems & Perspectives, volume 4 of *Springer Proceedings in Mathematics*, pages 1035–1042. Springer Berlin Heidelberg, 2011. 10.1007/978-3-642-20671-9_101.

- [9] H. Nilsen, K.-A. Lie, and J. Natvig. Accurate modelling of faults by multipoint, mimetic, and mixed methods. *SPE Journal*, 17(2), 2012.

Appendix A

The Curved Mimetic Finite-Difference module for MRST

In this appendix we present how to obtain the implementation of the curved mimetic method, and give a tutorial to the implementation.

A.1 The implementation in MATLAB

All implementations in this thesis is done using the MATLAB Reservoir Simulation Toolbox (MRST). The main parts of the code for the curved mimetic method has been made available as a module for MRST.¹

A.2 Tutorial for the CMFD module

This tutorial is largely based on the MRST tutorial found here: <http://www.sintef.no/Projectweb/MRST/Tutorials/Flow-Solver-Tutorial/>

The purpose of this example is to give an overview of how to set up and use the single-phase curved mimetic pressure solver to solve the single-phase pressure equation

$$\nabla \cdot v, \quad v = -\frac{K}{\mu} \nabla p \quad (\text{A.1})$$

for a flow driven by Dirichlet and Neumann boundary conditions. Our geological model will be simple; a perturbed Cartesian (curvilinear) grid with

¹To obtain the module, contact SINTEF thorough <http://www.sintef.no/MRST>.

isotropic, homogeneous permeability.

Define geometry

Construct a Cartesian grid of size 10-by-10-by-4 cells, where each cell has dimension 1-by-1-by-1. Because our flow solvers are applicable for general unstructured grids, the Cartesian grid is here represented using an unstructured format, in which cells, faces, nodes, etc. are given explicitly.

```
nx = 10; ny = 10; nz = 4;
G = cartGrid([nx, ny, nz]);
```

Then the nodes of the grid is perturbed so that the inner faces are curved, but the global shape of the reservoir is unchanged.

```
G = perturbate(G,nx,ny,nz,false,0.5);
display(G);
```

After the grid structure is generated, we plot the geometry.

```
plotGrid(G);
view(3), camproj orthographic, axis tight, camlight headlight
```

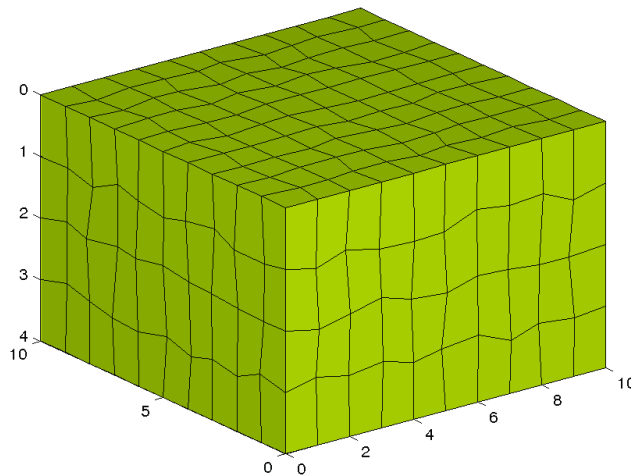


Figure A.1: Plot of the grid.

Process geometry

Having set up the basic structure, we continue to compute centroids and volumes of the cells and centroids, normals, and areas for the faces. For a Cartesian grid, this information can trivially be computed, but is given explicitly so that the flow solver is compatible with fully unstructured grids.

```
G = computeGeometry(G);
```

The mimetic method uses one degree of freedom for the flux over each face. In the curved mimetic method, two extra degrees of freedom for the velocity are added for each face. These new unknowns are associated with the flow orthogonal to the normal direction. We therefore compute orthogonal vectors \mathbf{a}_2 and \mathbf{a}_3 for each face. A plot of a single grid cell and the normal and orthogonal vectors are shown and the relevant constants needed are calculated.

```
tutorialGridCell
```

```
G = computeCmatrix(G);
```

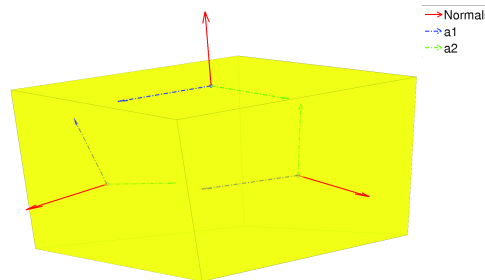


Figure A.2: Plot of a grid cell with curved faces and the normal and orthonormal vectors.

Set rock and fluid data

The only parameters in the single-phase pressure equation are the permeability and the fluid viscosity. We set the permeability to be homogeneous and

isotropic. The viscosity is specified by saying that the reservoir is filled with a single fluid, for which the default viscosity value equals unity. Our flow solver is written for a general incompressible flow and requires the evaluation of a total mobility, which is provided by the `fluid` object.

```
rock.perm = repmat(100*milli*darcy(), [G.cells.num, 1]);

fluid      = initSingleFluid('mu' ,    1*centi*poise      , ...
                             'rho', 1014*kilogram/meter^3);
```

For heterogeneous permeability we calculate the constants needed for the new continuity condition. This step is not necessary for the homogeneous case, where the naive continuity condition and the new continuity condition are the same. Note that the method only is valid for isotropic permeability, or permeabilities that has the same anisotropy rate for the entire reservoir, i.e., that satisfy Equation (3.53).

```
G = makeKalpha(G, rock);
```

Initialize reservoir simulator

To simplify communication among different flow and transport solvers, all unknowns are collected in a structure. Here this structure is initialized with uniform initial reservoir pressure equal 0 and (single-phase) saturation equal 0.0 (using the default behavior of `initResSol`).

```
resSol = initResSol(G, 0.0);
display(resSol);
```

Impose Dirichlet boundary conditions

Our flow solvers automatically assume no-flow conditions on all outer (and inner) boundaries; other type of boundary conditions need to be specified explicitly. Here, we impose Neumann conditions (flux of 1 m³/day) on the global left-hand side. The fluxes must be given in units of m³/s, and thus we need to divide by the number of seconds in a day. Similarly, we set Dirichlet boundary conditions $p = 0$ on the global right-hand side of the grid, respectively. For a single-phase flow, we need not specify the saturation at inflow boundaries. Similarly, fluid composition over outflow faces (here, right) is ignored by `pside`.

```
bc = fluxside([], G, 'LEFT', 1*meter^3/day());
bc = pside    (bc, G, 'RIGHT', 0);
display(bc);
```

Construct linear system

Construct mimetic pressure linear system components for the system $Ax = b$ where $B1$, C , $D1$ are the same as for the mimetic method and $E1 = D1$. For the homogeneous case, $E2 = D2$ and $E3 = D3$, but for the new continuity condition, the $E2$ and $E3$ contain the ratio of permeability, computed by `makeKalpha.m`. $v1$ is the flux and $cp1$ the face pressures, as in the mimetic method. $v2$, $v3$, $cp2$ and $cp3$ are new unknowns associated with the orthogonal vectors $a2$ and $a3$ as in the figure from `tutorialGridCell`.

$$A = \begin{bmatrix} B1 & 0 & 0 & C & D1 & 0 & 0 \\ 0 & B2 & 0 & 0 & 0 & D2 & 0 \\ 0 & 0 & B3 & 0 & 0 & 0 & D3 \\ C' & 0 & 0 & 0 & 0 & 0 & 0 \\ E1' & 0 & 0 & 0 & 0 & 0 & 0 \\ 0 & E2' & 0 & 0 & 0 & 0 & 0 \\ 0 & 0 & E3' & 0 & 0 & 0 & 0 \end{bmatrix} \begin{bmatrix} v1 \\ v2 \\ v3 \\ -p \\ cp1 \\ cp2 \\ cp3 \end{bmatrix} = \begin{bmatrix} f1 \\ f2 \\ f3 \\ g \\ h1 \\ h2 \\ h3 \end{bmatrix} = b.$$

The A matrix and the b vector is constructed based on input grid and rock properties for the case with no gravity.

```
gravity off;
S = computeCurMimeticIP(G, rock);
```

Plot the structure of the matrix (here we use BI , the inverse of B , rather than B)

```
clf, subplot(1,2,1)
cellNo = rldecode(1:G.cells.num, diff(G.cells.facePos), 2) .';
C = sparse(1:numel(cellNo), cellNo, 1);
D = sparse(1:numel(cellNo), double(G.cells.faces(:,1)), 1, ...
           numel(cellNo), G.faces.num);

C = [C;zeros(2*S.ncuF,G.cells.num)];
D = blkdiag(D,D(S.cuF,G.faces.cufg),D(S.cuF,G.faces.cufg));

spy([S.BI           , C           , D           ; ...
     C', zeros(size(C,2), size(C,2) + size(D,2)); ...
     D', zeros(size(D,2), size(C,2) + size(D,2))]);
title('Hybrid pressure system matrix')
```

The block structure can clearly be seen in the sparse matrix A, which is never formed in full. Indeed, rather than storing B, we store its inverse B^{-1} . Similarly, the C and D blocks are not represented in the S structure; they can easily be formed explicitly whenever needed, or their action can easily be computed.

```
display(S);
```

Solve the linear system

Solve linear system constructed from S and bc to obtain solution for flow and pressure in the reservoir. The option 'MatrixOutput=true' adds the system matrix A to resSol to enable inspection of the matrix.

```
resSol = solveIncompFlowCMFD(resSol, G, S, fluid, ...
                             'bc', bc, 'MatrixOutput', true);
display(resSol);
```

Inspect results

The resSol object contains the Schur complement matrix used to solve the hybrid system.

```
subplot(1,2,2), spy(resSol.A);
title('Schur complement system matrix');
```

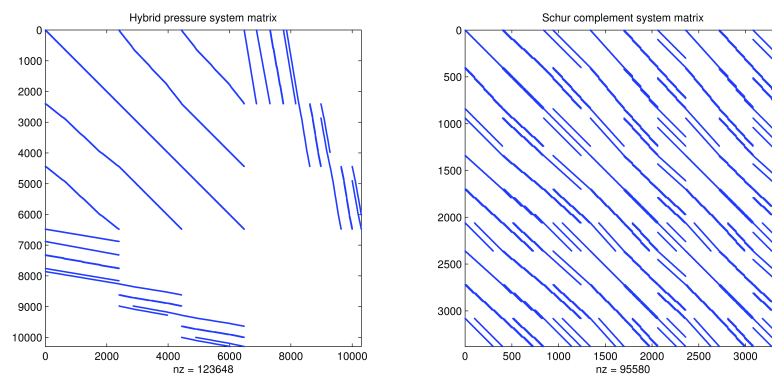


Figure A.3: Spy plot of the system matrix and the schur complement.

We then convert the computed pressure to unit 'bar' before plotting result.

```
figure
plotCellData(G, convertTo(resSol.pressure(1:G.cells.num), barsa()), ...
             'EdgeColor', 'k');
title('Cell Pressure [bar]')
xlabel('x'), ylabel('y'), zlabel('Depth');
view(3); shading faceted; camproj perspective; axis tight;
colorbar
```

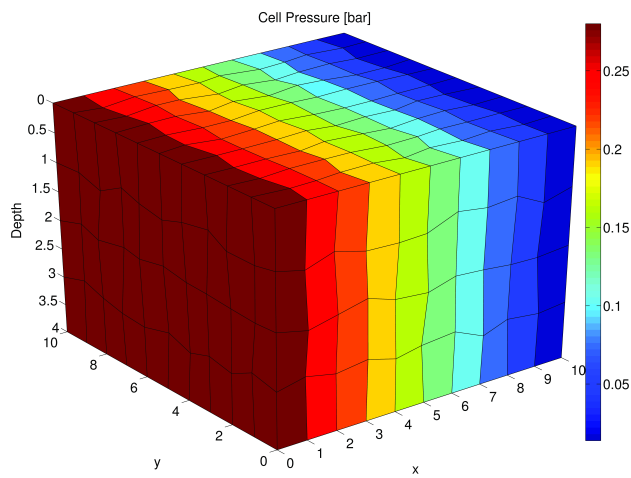


Figure A.4: Plot of the pressure solution.